Article

Neuron

GABAergic Neuron-Specific Loss of *Ube3a* Causes Angelman Syndrome-Like EEG Abnormalities and Enhances Seizure Susceptibility

Highlights

- Glutamatergic *Ube3a* loss decreases tonic inhibition onto L2/3 pyramidal neurons
- GABAergic *Ube3a* loss does not compromise inhibition onto L2/3 pyramidal neurons
- GABAergic, not glutamatergic, *Ube3a* loss causes EEG abnormalities and seizures
- L2/3 GABAergic defects in AS mice neither cause, nor are caused by, seizures

Authors

Matthew C. Judson, Michael L. Wallace, Michael S. Sidorov, ..., Ype Elgersma, Richard J. Weinberg, Benjamin D. Philpot

Correspondence

bphilpot@med.unc.edu

In Brief

Judson and colleagues use neuron-type-specific manipulations of maternal *Ube3a* expression to demonstrate that GABAergic *Ube3a* loss is sufficient to yield Angelman syndrome-like EEG abnormalities, enhancements in seizure susceptibility, and atypical clathrin-coated vesicle accumulations within presynaptic terminals.

Judson et al., 2016, Neuron *90*, 56–69
April 6, 2016 ©2016 Elsevier Inc.
http://dx.doi.org/10.1016/j.neuron.2016.02.040

CellPress

CellPress

Neuron
Article

GABAergic Neuron-Specific Loss of *Ube3a* Causes Angelman Syndrome-Like EEG Abnormalities and Enhances Seizure Susceptibility

Matthew C. Judson,[1,3,9] Michael L. Wallace,[2,3,8,9] Michael S. Sidorov,[1,3] Alain C. Burette,[1] Bin Gu,[1,3] Geeske M. van Woerden,[4,5] Ian F. King,[6] Ji Eun Han,[1] Mark J. Zylka,[1,2,3,7] Ype Elgersma,[4,5] Richard J. Weinberg,[1,2] and Benjamin D. Philpot[1,2,3,7,*]

[1]Department of Cell Biology and Physiology
[2]Curriculum in Neurobiology
[3]Carolina Institute for Developmental Disabilities
University of North Carolina, Chapel Hill, NC 27599, USA
[4]Department of Neuroscience
[5]*ENCORE* Center for Neurodevelopmental Disorders
Erasmus Medical Center, Wytemaweg 80, 3015 CN Rotterdam, the Netherlands
[6]Department of Pathology and Laboratory Medicine
[7]Neuroscience Center
University of North Carolina, Chapel Hill, Chapel Hill, NC 27599, USA
[8]Present address: Department of Neurobiology, Harvard Medical School, Boston, MA 02115, USA
[9]Co-first author
*Correspondence: bphilpot@med.unc.edu
http://dx.doi.org/10.1016/j.neuron.2016.02.040

SUMMARY

Loss of maternal *UBE3A* causes Angelman syndrome (AS), a neurodevelopmental disorder associated with severe epilepsy. We previously implicated GABAergic deficits onto layer (L) 2/3 pyramidal neurons in the pathogenesis of neocortical hyperexcitability, and perhaps epilepsy, in AS model mice. Here we investigate consequences of selective *Ube3a* loss from either GABAergic or glutamatergic neurons, focusing on the development of hyperexcitability within L2/3 neocortex and in broader circuit and behavioral contexts. We find that GABAergic *Ube3a* loss causes AS-like increases in neocortical EEG delta power, enhances seizure susceptibility, and leads to presynaptic accumulation of clathrin-coated vesicles (CCVs)—all without decreasing GABAergic inhibition onto L2/3 pyramidal neurons. Conversely, glutamatergic *Ube3a* loss fails to yield EEG abnormalities, seizures, or associated CCV phenotypes, despite impairing tonic inhibition onto L2/3 pyramidal neurons. These results substantiate GABAergic *Ube3a* loss as the principal cause of circuit hyperexcitability in AS mice, lending insight into ictogenic mechanisms in AS.

INTRODUCTION

Angelman syndrome (AS) is a debilitating neurodevelopmental disorder defined by severe developmental delay, movement disorders, profound speech impairment, and highly penetrant electroencephalographic (EEG) abnormalities and seizures (Williams et al., 2006; Thibert et al., 2013). The frequency, severity, and intractability of the seizures exact a heavy toll on the quality of life of individuals with AS and their caregivers (Thibert et al., 2013). Loss of function of the maternal *UBE3A* allele causes AS (Kishino et al., 1997; Matsuura et al., 1997; Sutcliffe et al., 1997). *UBE3A* encodes an E3 ubiquitin ligase, which catalyzes the transfer of ubiquitin to substrate proteins, thereby targeting them for proteasomal degradation or otherwise altering their localization or function (Rotin and Kumar, 2009; Mabb and Ehlers, 2010; Mabb et al., 2011). Because mutations that selectively inhibit UBE3A ligase activity are sufficient to cause AS, improper ubiquitin substrate regulation likely contributes to the pathogenesis of the disorder (Cooper et al., 2004). Unlike other cells, neurons express UBE3A exclusively from the maternal allele due to evolutionarily conserved, cell-type-specific epigenetic mechanisms that silence the paternal *UBE3A* allele (Rougeulle et al., 1997; Yamasaki et al., 2003; Judson et al., 2014). Accordingly, neurons are especially vulnerable to loss of maternal *UBE3A*.

Previously, we utilized a maternal *Ube3a*-null ($Ube3a^{m-/p+}$) mouse model of AS (Jiang et al., 1998) to explore the neural basis of hyperexcitability phenotypes in the disorder. We discovered that severe reduction of inhibitory GABAergic input to layer (L) 2/3 pyramidal neurons outweighs corresponding losses of excitatory glutamatergic input, possibly contributing to neocortical hyperexcitability. Recovery of inhibitory synaptic transmission following high-frequency stimulation is severely compromised and is associated with accumulations of clathrin-coated vesicles (CCVs) at GABAergic presynaptic terminals onto L2/3 pyramidal neurons (Wallace et al., 2012). Maternal *Ube3a* deficiency may thus disrupt presynaptic vesicle cycling in GABAergic neurons, possibly through the dysregulation of UBE3A substrates that

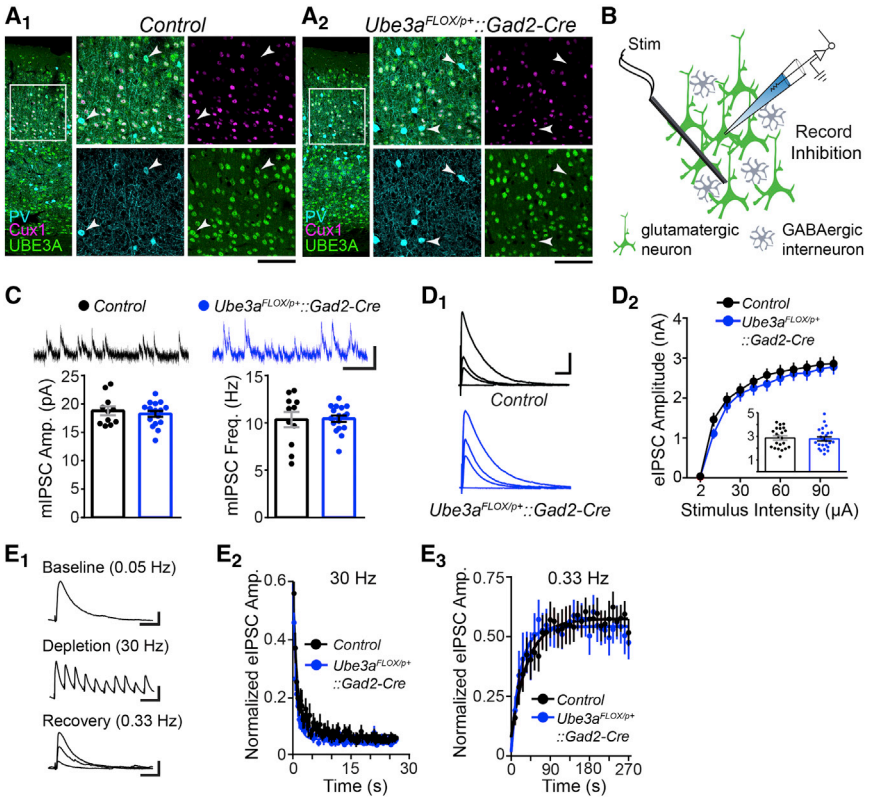

Figure 1. GABAergic *Ube3a* Loss Does Not Compromise Synaptic Inhibition onto L2/3 Pyramidal Neurons

(A) Immunostaining of parvalbumin (PV), Cux1, and UBE3A in V1 of ~P80 *Control* (A_1) and *Ube3a*$^{FLOX/p+}$*::Gad2-Cre* (A_2) mice. Arrowheads indicate PV-positive interneurons, which lack UBE3A in *Ube3a*$^{Flox/p+}$*::Gad2-Cre* mice (scale bar: 145 μm or 75 μm for zoom-ins).

(B) Schematic for recording synaptic inhibition onto L2/3 pyramidal neurons in V1 of ~P80 *Ube3a*$^{FLOX/p+}$*::Gad2-Cre* mice (green shading indicates presence of UBE3A).

(C) Sample recordings (scale bar: 20 pA, 200 ms) and quantification of mIPSC amplitude and frequency (*Control* n = 11 cells; *Ube3a*$^{FLOX/p+}$*::Gad2-Cre* n = 17 cells).

(D) Sample recordings of eIPSCs (D_1) at stimulation intensities of 2, 10, 30, and 100 μA (scale bar: 1 nA, 40 ms). (D_2) Quantification of eIPSCs. Inset depicts response amplitudes to 100 μA stimulation (*Control* n = 22 cells; *Ube3a*$^{FLOX/p+}$*::Gad2-Cre* n = 24 cells).

(E) Sample recordings (E_1) depicting each phase of an inhibitory synaptic depletion and recovery experiment (scale bars: baseline = 200 pA, 20 ms; depletion = 200 pA, 70 ms; recovery = 200 pA, 20 ms). (E_2) Average depletion phase showing eIPSC amplitude normalized to baseline during 800 stimuli at 30 Hz. Each point (80 plotted per genotype) represents ten consecutive responses that were collapsed and averaged per cell. (E_3) Average recovery phase showing eIPSC amplitude normalized to baseline during 90 stimuli at 0.33 Hz. Each point (30 plotted per genotype) represents three consecutive responses that were collapsed and averaged per cell. Average depletion and recovery responses for each genotype were fit with a monophasic exponential (*Control* n = 11 cells; *Ube3a*$^{FLOX/p+}$*::Gad2-Cre* n = 9 cells). Data represent mean ± SEM.

directly or indirectly compromise clathrin-mediated endocytosis. Conversely, it is possible that loss of maternal *Ube3a* expression in glutamatergic neurons compromises the postsynaptic effects of GABA on L2/3 pyramidal neurons, thereby contributing to hyperexcitability within the microcircuit and throughout the brain. In support of this latter possibility, modulation of expression or activity levels of ARC or the calcium/calmodulin-dependent kinase type II-α subunit (CaMKII-α)—both of which are preferentially expressed by glutamatergic forebrain neurons—has been shown to rescue circuit hyperexcitability and seizures in *Ube3a*$^{m-/p+}$ mice (van Woerden et al., 2007; Mandel-Brehm et al., 2015). Thus, an immediate goal is to determine whether maternal *Ube3a* loss restricted to either GABAergic or glutamatergic neurons is sufficient to impair GABAergic inhibition onto L2/3 pyramidal neurons, thereby leading to broader circuit-level and behavioral manifestations of hyperexcitability.

Here we utilize novel conditional *Ube3a* mouse models to identify the neurons and neural circuits underlying the pathogenesis of circuit hyperexcitability in AS. We focus on selective *Ube3a* loss from GABAergic or glutamatergic neurons, which are largely responsible for orchestrating the balance between excitation and inhibition in cerebral circuits. Our results provide compelling evidence that GABAergic, but not glutamatergic, *Ube3a* loss is responsible for mediating the EEG abnormalities and seizures that affect individuals with AS.

RESULTS

GABAergic *Ube3a* Loss Does Not Impair GABAergic Neurotransmission onto L2/3 Pyramidal Neurons

To enable genetic dissection of neuron-type-specific contributions to circuit hyperexcitability in AS, we generated a novel mouse with maternal inheritance of a floxed *Ube3a* allele (*Ube3a*$^{FLOX/p+}$) (Figure S1). We first crossed *Ube3a*$^{FLOX/p+}$ mice to a *Gad2-Cre* line in which Cre is expressed by almost all inhibitory GABAergic neurons throughout the brain (Taniguchi et al., 2011). We immunohistochemically confirmed loss of UBE3A expression by GABAergic interneurons in adult *Ube3a*$^{FLOX/p+}$*::Gad2-Cre* mice, including parvalbumin-expressing subtypes in primary visual cortex (V1) (Figure 1A_2). The density of these interneuron subtypes in V1 was normal (Figure S2A), indicating that GABAergic *Ube3a* loss does not grossly disrupt GABAergic neuronal architecture in the neocortex. Moreover, GABAergic *Ube3a* loss in *Ube3a*$^{FLOX/p+}$*::Gad2-Cre* mice proved to be selective, as UBE3A co-staining with the L2–4 glutamatergic neuron marker, Cux1 (Nieto et al., 2004), was intact (Figures 1A_1 and 1A_2).

We then sought to determine if GABAergic neuron-specific loss of maternal *Ube3a* is sufficient to alter synaptic drive onto L2/3 pyramidal neurons, testing *Ube3a*$^{FLOX/p+}$*::Gad2-Cre* mice for the same spectrum of synaptic defects that we had previously observed in V1 of AS model mice (*Ube3a*$^{m-/p+}$)

(Wallace et al., 2012). As expected, we found no difference in mEPSC amplitude or frequency onto L2/3 pyramidal neurons in *Ube3a*$^{FLOX/p+}$*::Gad2-Cre* compared to *Control* mice (Figure S2B). We also observed normal mIPSC amplitude and frequency in *Ube3a*$^{FLOX/p+}$*::Gad2-Cre* mice (Figure 1C), indicating that spontaneous GABAergic synaptic transmission remains intact following GABAergic neuron-specific loss of maternal *Ube3a*. This was unexpected, in view of previous evidence that decreased mIPSC frequency is a core GABAergic synaptic defect onto L2/3 pyramidal neurons in *Ube3a*$^{m-/p+}$ mice (Table 1) (Wallace et al., 2012).

We were even more surprised to find that GABAergic *Ube3a* loss yields neither of two core deficits in electrically evoked inhibition observed in *Ube3a*$^{m-/p+}$ mice: decreased evoked inhibitory postsynaptic current (eIPSC) amplitude or blunted recovery of GABAergic synaptic responses following high-frequency stimulation (Table 1). By stimulating (150 μm inferior to the recorded neuron) at a range of intensities, we revealed that eIPSC response amplitudes in *Ube3a*$^{FLOX/p+}$*::Gad2-Cre* mice are equivalent to *Control* (Figure 1D), indicating that the strength of GABAergic inputs onto L2/3 pyramidal neurons develops normally following GABAergic *Ube3a* loss. To test the recovery of GABAergic synaptic transmission following high-frequency stimulation, we applied a train of 800 stimuli at 30 Hz to deplete reserves of GABAergic vesicles, followed immediately by 0.33 Hz stimulation to allow for recovery (Figure 1E1). We recorded eIPSC amplitudes from L2/3 pyramidal neurons during both phases of this experiment, to gauge rates of GABAergic synaptic depletion and recovery. Depletion of eIPSC amplitude in *Ube3a*$^{FLOX/p+}$*::Gad2-Cre* mice was equivalent to *Control* (Figure 1E2), as was recovery (Figure 1E3). Although eIPSC paired-pulse ratio in *Ube3a*$^{FLOX/p+}$*::Gad2-Cre* mice was subtly decreased when stimulating with a 100 ms inter-stimulus interval (ISI), eIPSC paired-pulse with 33 ms ISI was normal (Figure S2C). Thus, short-term plasticity at this synapse is largely intact following GABAergic *Ube3a* loss, particularly in response to the stimulation frequency we used to deplete GABAergic synapses (Figure 1E$_2$).

Importantly, nervous system-wide deletion of *Ube3a*$^{FLOX/p+}$ (*Ube3a*$^{FLOX/p+}$*::Nestin-Cre*) produced a loss of *Ube3a* expression that was indistinguishable from *Ube3a* loss in *Ube3a*$^{m-/p+}$ mice (Figure S3); moreover, *Ube3a*$^{FLOX/p+}$*::Nestin-Cre* mice closely phenocopied L2/3 GABAergic synaptic defects in *Ube3a*$^{m-/p+}$ mice (Table 1; Figure S4). *Ube3a*^{FLOX} thus appears to be a viable conditional null allele, supporting the lack of phenotypic penetrance in *Ube3a*$^{FLOX/p+}$*::Gad2-Cre* mice as a genuine finding, rather than an artifact of residual *Ube3a* function following *Gad2-Cre*-mediated deletion. Collectively, these observations indicate that GABAergic *Ube3a* loss does not severely impair GABAergic synaptic drive onto L2/3 pyramidal neurons as results from *Ube3a* loss in all neurons (Table 1).

Glutamatergic *Ube3a* Loss Impairs Electrically Evoked and Tonic GABAergic Inhibition onto L2/3 Pyramidal Neurons

To model glutamatergic *Ube3a* loss in a manner truly reciprocal to GABAergic *Ube3a* loss in *Ube3a*$^{FLOX/p+}$*::Gad2-Cre* mice, we crossed conditional *Ube3a* reinstatement mice (*Ube3a*$^{STOP/p+}$) to the same *Gad2-Cre* line. *Ube3a*$^{STOP/p+}$ mice constitute a conditional AS model in which expression of the maternal *Ube3a* allele is interrupted by targeted insertion of a floxed STOP cassette. Cre-mediated excision of the STOP cassette fully reinstates neuronal UBE3A expression in *Ube3a*$^{STOP/p+}$ mice (Silva-Santos et al., 2015). Hence, when we crossed *Ube3a*$^{STOP/p+}$ mice to *Gad2-Cre* mice (*Ube3a*$^{STOP/p+}$*::Gad2-Cre)*, we observed UBE3A reinstatement that was specific to GABAergic interneurons in the neocortex, leaving neighboring Cux1-expressing glutamatergic neurons devoid of UBE3A expression in L2/3 neocortex (Figure 2A). Thus, *Ube3a*$^{STOP/p+}$*::Gad2-Cre* mice are an appropriate model of glutamatergic *Ube3a* loss.

To evaluate whether glutamatergic *Ube3a* loss in *Ube3a*$^{STOP/p+}$*::Gad2-Cre* mice could impair GABAergic synaptic drive onto L2/3 pyramidal neurons, we first needed to determine the extent to which *Ube3a*$^{STOP/p+}$ mice recapitulated key GABAergic synaptic defects. We found that *Ube3a*$^{STOP/p+}$ mice closely phenocopied *Ube3a*$^{m-/p+}$ and *Ube3a*$^{FLOX/p+}$*::Nestin-Cre* mice with respect to reduced eIPSC amplitude (Figure 2C) and blunted recovery from inhibitory synaptic depletion (Figure 2D). However, *Ube3a*$^{STOP/p+}$ mice failed to exhibit mIPSC amplitude or frequency deficits despite our experimentation with near-physiological as well as increased intracellular chloride levels (Figures S5B and S5C). It is possible that *Ube3a*^{STOP} allele readthrough provided enough *Ube3a* expression, albeit very low (Silva-Santos et al., 2015), to selectively mitigate penetrance of the mIPSC deficit. Regardless of the underlying reason for this result, we were limited to evaluating only eIPSC amplitude and GABAergic synaptic recovery in *Ube3a*$^{STOP/p+}$*::Gad2-Cre* mice.

Ube3a$^{STOP/p+}$*::Gad2-Cre* mice proved to be statistically indistinguishable from *Ube3a*$^{STOP/p+}$ (but also *Control*) mice on measures of eIPSC amplitude (Figure 2C), providing a clue that glutamatergic *Ube3a* loss diminishes L2/3 pyramidal neuron responses to evoked GABAergic neurotransmission. Similar to *Ube3a*$^{STOP/p+}$ and *Control* mice, *Ube3a*$^{STOP/p+}$*::Gad2-Cre* mice showed no impairment on measures of mEPSCs, eIPSC paired-pulse ratios, or inhibitory synaptic depletion dynamics (Figures S5A, S5D, S5E$_1$, and S5E$_2$). In contrast, the blunted recovery from GABAergic synaptic depletion that we observed in *Ube3a*$^{STOP/p+}$ mice was completely absent in *Ube3a*$^{STOP/p+}$*::Gad2-Cre* mice (Figure 2D). This result demonstrates that glutamatergic *Ube3a* loss, just like GABAergic *Ube3a* loss (Figure 1E), fails to impair GABAergic synaptic recovery from high-frequency stimulation.

Selective manipulations of glutamatergic *Ube3a* expression in the neocortex should affect the penetrance of eIPSC amplitude deficits, assuming these deficits are secondary to an intrinsic loss of UBE3A function within L2/3 pyramidal neurons. We tested this assumption with several approaches. First, we crossed *Ube3a*$^{STOP/p+}$ mice to a NEX-*Cre* line (*Ube3a*$^{STOP/p+}$*::NEX-Cre*) in which *Ube3a* is selectively reinstated in glutamatergic neurons of the dorsal pallium, including Cux1-positive neurons of L2/3 neocortex (Figure 3A$_3$). eIPSC amplitudes in *Ube3a*$^{STOP/p+}$*::NEX-Cre* mice were similar to *Control* (Figures 3B and 3C), supporting that this deficit in *Ube3a*$^{STOP/p+}$ mice is driven by glutamatergic, not GABAergic, *Ube3a* loss in L2/3 neocortex, in agreement with our findings from *Ube3a*$^{FLOX/p+}$*::Gad2-Cre* mice (Figure 1D). To further demonstrate the neuron

Table 1. Summary of Neocortical Inhibitory Synaptic Defects, EEG Abnormalities, and Behavioral Seizure Phenotypes in *Ube3a* Mice

		GABAergic Synaptic Defects onto L2/3 Pyramidal Neurons					
Mouse Model	UBE3A Expression Deficit	mIPSC Freq.	eIPSC Amp.	Inhibitory Synaptic Recovery	Inhibitory Presynaptic CCVs	Intracortical EEG	Behavioral Seizure Phenotype
Ube3a$^{m-/p+}$	deleted in all neurons	↓49%[a]	↓43%[a]	↓30%[a]	↑214%[a]	electrographic seizures, polyspike and slow wave discharges[b]	spontaneous: yes[b]; flurothyl: NA; AGS: enhanced susceptibility[b,c]
Ube3a$^{FLOX/p+}$*:: Nestin-Cre*	deleted in all neurons	↓25%	↓18%	↓18%	↑124%	NA	NA
Ube3a$^{STOP/p+}$	suppressed in all neurons	↔	↓20%	↓32%	↑222%	enhanced delta power	spontaneous: not observed; flurothyl: NA; AGS: enhanced susceptibility[d]
Ube3a$^{FLOX/p+}$*:: Gad2-Cre*	deleted in nearly all GABAergic neurons	↔	↔	↔	↑116%	enhanced delta power	spontaneous: yes, enhanced postnatal lethality; flurothyl: decreased latency, enhanced lethality; AGS: enhanced susceptibility, severe
Ube3a$^{STOP/p+}$*:: Gad2-Cre*	suppressed in all glutamatergic neurons and other non-GABAergic neurons	↔	↓10%[e]	↔	↔	normal spectral power	spontaneous: not observed; flurothyl: NA; AGS: not susceptible
Ube3a$^{FLOX/p+}$*:: NEX-Cre*	deleted in glutamatergic neurons of dorsal pallial origin	↔	↓25%	↔	NA	NA	spontaneous: not observed; flurothyl: normal susceptibility; AGS: NA

↔, equivalent to Control; ↑, increased relative to Control; ↓, decreased relative to Control; NA, Not Assayed; AGS, audiogenic seizure.

[a]Wallace et al. (2012).

[b]Jiang et al. (1998).

[c]van Woerden et al. (2007).

[d]Silva-Santos et al. (2015).

[e]Did not reach statistical significance.

CellPress

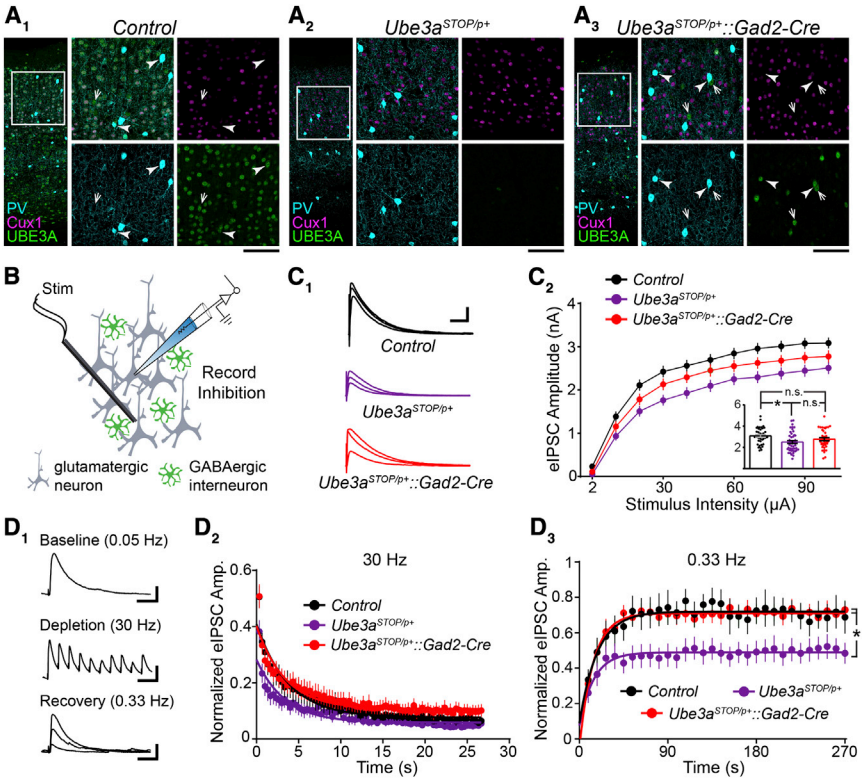

Figure 2. GABAergic *Ube3a* Reinstatement in *Ube3a*$^{STOP/p+}$*::Gad2-Cre* Mice Models Glutamatergic *Ube3a* Loss and Indicates an Evoked IPSC Amplitude Deficit onto L2/3 Pyramidal Neurons

(A) Immunostaining of parvalbumin (PV), Cux1, and UBE3A in V1 of ~P80 *Control* (A_1); *Ube3a*$^{STOP/p+}$ (A_2); and *Ube3a*$^{STOP/p+}$*::Gad2-Cre* (A_3) mice. Arrowheads indicate PV-positive interneurons that co-stain for UBE3A. Arrows point to PV-negative interneurons that co-stain for UBE3A (scale bar: 145 μm or 75 μm for zoom-ins).

(B) Schematic for recording synaptic inhibition onto L2/3 pyramidal neurons in V1 of ~P80 *Ube3a*$^{STOP/p+}$*::Gad2-Cre* mice.

(C) Sample recordings of eIPSCs (C_1) at stimulation intensities of 2, 10, 30, and 100 μA (scale bar: 1 nA, 60 ms). (C_2) Quantification of eIPSCs. Inset depicts response amplitudes to 100 μA stimulation (*Control* n = 38 cells; *Ube3a*$^{STOP/p+}$ n = 44 cells; *Ube3a*$^{STOP/p+}$*::Gad2-Cre* n = 40 cells).

(D) Inhibitory synaptic depletion and recovery in *Control* (n = 9 cells), *Ube3a*$^{STOP/p+}$ (n = 11 cells), and *Ube3a*$^{STOP/p+}$*::Gad2-Cre* (n = 13 cells) mice, performed as in Figure 1E. Scale bars (D_1): baseline = 200 pA, 20 ms; depletion = 200 pA, 70 ms; recovery = 200 pA, 20 ms. Data represent mean ± SEM. *p ≤ 0.05.

type specificity of this phenotype, we probed *Ube3a*$^{FLOX/p+}$*::NEX-Cre* mice (Figure 3A_4), observing that neocortical glutamatergic *Ube3a* deletion was sufficient to yield the eIPSC deficit (Figures 3D and 3E). Finally, to test the cell autonomy of the effect, we intracerebroventricularly delivered low titers of Cre-expressing adeno-associated virus (AAV-Cre) to neonatal *Ube3a*$^{FLOX/p+}$ and *Ube3a*$^{m+/p+}$ control littermates (Figure S6A_1). This produced a sparse mosaic of virally transduced neocortical neurons, including pyramidal neurons, which we identified by expression of a Cre-dependent tdTomato reporter. We observed a total loss of UBE3A expression in over 80% of tdTomato-positive neurons in *Ube3a*$^{FLOX/p+}$ mice by P12 (Figures S6A_3 and S6A_4). Conversely, almost all (>90%) tdTomato-positive neurons expressed UBE3A in *Ube3a*$^{m+/p+}$ littermates (Figures S6A2 and S6A4). We measured eIPSC amplitude in mice prepared in this manner at ~P80, recording from tdTomato-positive L2/3 pyramidal neurons (*Ube3a*$^{FLOX/p+}$*::AAV-Cre* or *Ube3a*$^{m+/p+}$*::AAV-Cre*), as well as neighboring non-transduced L2/3 pyramidal neurons (*Ube3a*$^{FLOX/p+}$ or *Ube3a*$^{m+/p+}$) in V1 (Figure S6B_1). We observed reduced eIPSC amplitude in response to a range of stimulation intensities in *Ube3a*$^{FLOX/p+}$*::AAV-Cre* neurons compared to *Ube3a*$^{m+/p+}$*::AAV-Cre*, *Ube3a*$^{FLOX/p+}$, or *Ube3a*$^{m+/p+}$ neurons (Figure S6B_2 and S6B_3). We therefore conclude that diminished eIPSC amplitude onto L2/3 pyramidal neurons in AS mice is due to cell-autonomous consequences of *Ube3a* loss.

Intriguingly, deficits in eIPSC amplitude in *Ube3a*$^{FLOX/p+}$*::NEX-Cre* mice occurred in the absence of changes in either mIPSC amplitude or frequency (Figure 3F), indicating that synaptic $GABA_A$R function may be normal following glutamatergic *Ube3a* deletion in the dorsal forebrain. This apparent phenotypic discrepancy may be explained by deficits in extrasynaptic, delta subunit-containing $GABA_A$Rs (δ-$GABA_A$Rs), which might only be revealed in instances of GABA spillover to extrasynaptic regions (for example, following strong electrical stimulation) (Wei et al., 2003). Because δ-$GABA_A$Rs are the principal mediators of tonic inhibition onto pyramidal neurons in the neocortex (Brickley and Mody, 2012), we reasoned that glutamatergic *Ube3a* loss might selectively impair this mode of GABAergic transmission by L2/3 pyramidal neurons. To test this, we bath-applied a δ-$GABA_A$R-selective concentration of THIP (Gaboxadol) to stimulate extrasynaptic $GABA_A$Rs, followed by a saturating concentration of the competitive $GABA_A$R antagonist, Gabazine (SR95531) (Figure 3G1). We recorded corresponding changes in holding current in L2/3 pyramidal neurons, finding that we could stimulate significantly less THIP/Gabazine-sensitive tonic current in *Ube3a*$^{FLOX/p+}$*::NEX-Cre* mice relative to *Control* (Figure 3G2). This effect was not an artifact of decreased cell size, as capacitances between the two genotypes were equivalent (Control n = 30 cells, 64.06 ± 3 pF; *Ube3a*$^{FLOX/p+}$*::NEX-Cre* n = 21 cells, 68.33 ± 4.71 pF; p = 0.43). Together, these observations support that glutamatergic *Ube3a* loss cell-autonomously impairs tonic GABAergic tone onto L2/3 pyramidal neurons.

GABAergic, but Not Glutamatergic, *Ube3a* Loss Enhances Seizure Susceptibility

Converging lines of evidence implicate deficits in tonic inhibition in the pathogenesis of epilepsy. In particular, *GABRD* missense mutations that reduce δ-$GABA_A$R-mediated currents

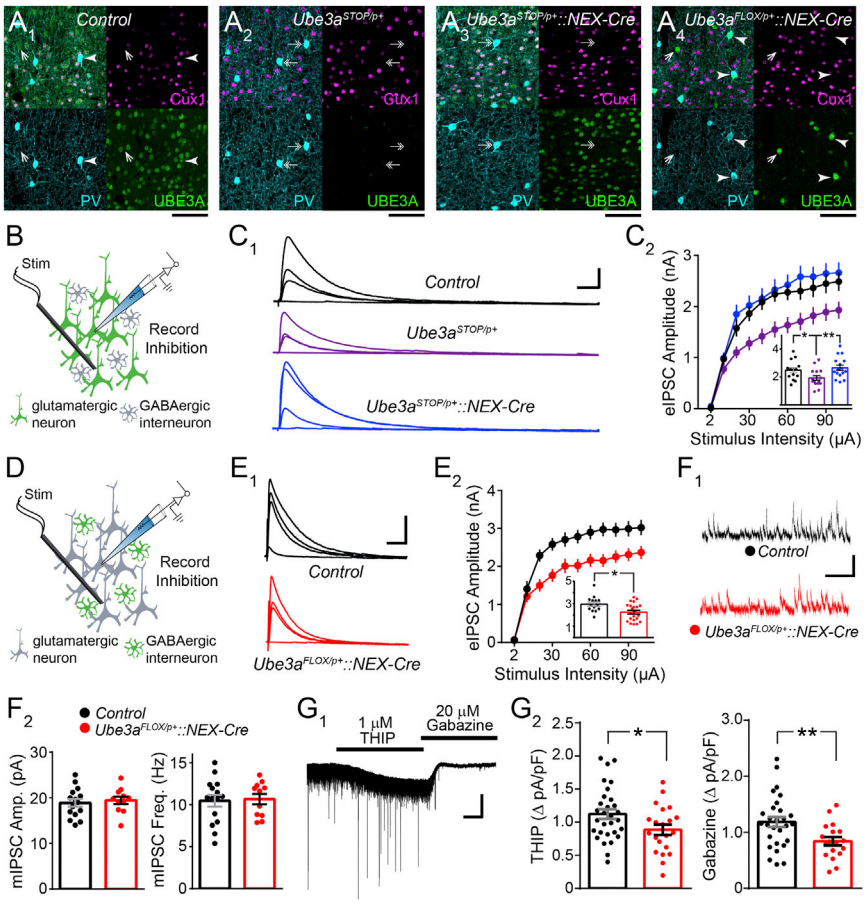

Figure 3. Glutamatergic *Ube3a* Loss Selectively Reduces Evoked IPSC Amplitude and Tonic Inhibitory Tone onto L2/3 Pyramidal Neurons

(A) Immunostaining of parvalbumin (PV), Cux1, and UBE3A in V1 of ~P80 *Control* (A_1); *Ube3a*$^{STOP/p+}$ (A_2); *Ube3a*$^{STOP/p+}$*::NEX-Cre* (A_3); and *Ube3a*$^{FLOX/p+}$*::NEX-Cre* (A_4) mice. Double arrows indicate PV-positive interneurons that lack UBE3A, arrowheads indicate PV-positive interneurons that co-stain for UBE3A but lack Cux1, and single arrows depict Cux1- and PV-negative interneurons that co-stain for UBE3A (scale bar: 75 μm for all panels).

(B) Schematic for recording inhibition onto L2/3 pyramidal neurons in V1 of ~P80 *Ube3a*$^{STOP/p+}$*::NEX-Cre* mice.

(C) Sample recordings of eIPSCs (C_1) at stimulation intensities of 2, 10, 30, and 100 μA (scale bar: 800 pA, 20 ms). (C_2) Quantification of eIPSCs. Inset depicts response amplitudes to 100 μA stimulation (*Control* n = 14 cells; *Ube3a*$^{STOP/p+}$ n = 15 cells; *Ube3a*$^{STOP/p+}$*::NEX-Cre* n = 16 cells).

(D) Schematic for recording inhibition onto L2/3 pyramidal neurons in V1 of ~P80 *Ube3a*$^{FLOX/p+}$*::NEX-Cre* mice.

(E) Sample recordings of eIPSCs (E_1) at stimulation intensities of 2, 10, 30, and 100 μA (scale bar: 1 nA, 40 ms). (E_2) Quantification of eIPSCs. Inset depicts response amplitudes to 80 μA stimulation (*Control* n = 14 cells; *Ube3a*$^{FLOX/p+}$*::NEX-Cre* n = 22 cells).

(F) Sample recordings ([F_1], scale bar: 20 pA, 200 ms) and quantification of mIPSC amplitude and frequency (F_2) (*Control* n = 15 cells; *Ube3a*$^{FLOX/p+}$*::NEX-Cre* n = 11 cells).

(G) Representative trace (G_1) from experiments to measure tonic inhibitory currents onto L2/3 pyramidal neurons (scale bar: 150 pA, 120 s). (G_2) Quantification of change in $I_{holding}$ in response to the application of the δ-$GABA_A$R agonist THIP (left) and the subsequent chase with the competitive $GABA_A$R antagonist, Gabazine (right) (*Control* n = 30 cells; *Ube3a*$^{FLOX/p+}$*::NEX-Cre* n = 21 cells). Data represent mean ± SEM. *p ≤ 0.05, **p ≤ 0.01.

are associated with generalized epilepsy in humans (Dibbens et al., 2004), and *Gabrd*$^{-/-}$ mice are prone to seizures (Spigelman et al., 2002; Maguire et al., 2005). Therefore, we hypothesized that deficits owed to glutamatergic *Ube3a loss*, including impaired tonic δ-$GABA_A$R-mediated inhibition onto pyramidal neurons, would correlate with enhanced seizure susceptibility.

Latencies to seizure following an initial exposure to the putative $GABA_A$R antagonist, flurothyl, provide a reliable index of seizure threshold in naive mice, and flurothyl seizures are highly penetrant regardless of genetic background (Krasowski, 2000; Kadiyala et al., 2014). We therefore used flurothyl to test seizure susceptibility in congenic C57BL/6 *Ube3a*$^{FLOX/p+}$*::NEX-Cre* mice (Figures 4A_1 and 4B). Surprisingly, we found that their latency to myoclonic and generalized seizure was similar to *Control* (Figure 4C). This finding indicates that decreased tonic GABAergic inhibition onto L2/3 pyramidal neurons does not confer vulnerability to seizures. Nor, in all likelihood, does any other physiological consequence of glutamatergic *Ube3a* loss in the dorsal telencephalon. In contrast, pan-cerebral GABAergic *Ube3a* loss on a congenic C57BL/6 background yielded a dramatic reduction in latency to myoclonus and generalized seizure, and even enhanced lethality to repeated (once daily) exposures to flurothyl, as evinced by experiments in *Ube3a*$^{FLOX/p+}$*::Gad2-Cre* mice (Figures 4A_2 and 4D).

Notably, *NEX-Cre* does not mediate glutamatergic *Ube3a* deletion in ventral neuron populations, nor in the majority of dentate granule neurons (Figure 4A_1) (Goebbels et al., 2006). Dentate granule neurons in particular receive an abundance of tonic GABAergic inhibition and are critical for gating temporal lobe excitability (Coulter and Carlson, 2007; Hsu, 2007; Pun et al., 2012), which might explain why *Ube3a*$^{FLOX/p+}$*::NEX-Cre* mice exhibit a normal response to flurothyl (Figure 4C). In contrast, *Ube3a*$^{STOP/p+}$*::Gad2-Cre* mice effectively model pan-cerebral glutamatergic *Ube3a* loss and thus provide a better model in which to fully evaluate the potential for glutamatergic *Ube3a* loss to enhance seizure susceptibility. As we maintain congenic 129S2/SvPasCrl *Ube3a*$^{STOP/p+}$ mice, we turned to a sensory-evoked, audiogenic seizure induction paradigm that is suited to assessing seizure susceptibility on this genetic background (Figure 5A). Importantly, the audiogenic seizure paradigm has previously been used to demonstrate enhanced seizure susceptibility in AS mouse models on a 129 background, including *Ube3a*$^{m-/p+}$ and *Ube3a*$^{STOP/p+}$ mice (Jiang et al., 1998; van Woerden et al., 2007; Silva-Santos et al., 2015).

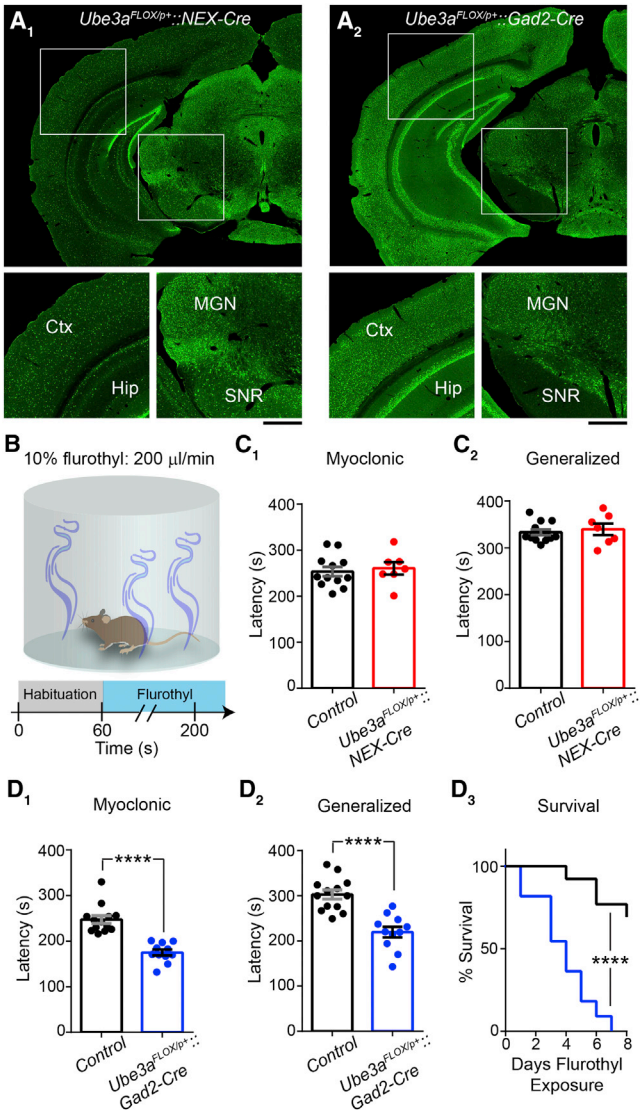

Figure 4. GABAergic, but Not Glutamatergic, *Ube3a* Loss Lowers the Threshold for Flurothyl-Induced Seizures

(A) UBE3A staining in *Ube3a*$^{FLOX/p+}$*::NEX-Cre* (A_1) and *Ube3a*$^{FLOX/p+}$*::Gad2-Cre* (A_2) (scale bar: 750 µm; 400 µm for zoom-ins). Ctx, cerebral cortex; Hip, hippocampus; MGN, medial geniculate thalamic nucleus; SNR, substantia nigra pars reticulata.

(B) Schematic of flurothyl-induced seizure protocol. Flurothyl administration ceases upon the occurrence of a generalized seizure.

(C) Latency to myoclonus (C_1) and generalized seizure (C_2) in *Control* (n = 12) and *Ube3a*$^{FLOX/p+}$*::NEX-Cre* (n = 7) mice at ~P80.

(D) Latency to myoclonus (D_1) and generalized seizure (D_2) in *Control* (n = 13) and *Ube3a*$^{FLOX/p+}$*::Gad2-Cre* (n = 11) mice at ~P80. Comparative survival (D_3) of *Control* and *Ube3a*$^{FLOX/p+}$*::Gad2-Cre* mice following repeated once daily exposures to flurothyl. Data represent mean ± SEM. ****p ≤ 0.0001.

We confirmed that 129S2/SvPasCrl *Ube3a*$^{STOP/p+}$ mice are much more susceptible to audiogenic seizures than their *Control* littermates in terms of both frequency and severity (Figure 5B). *Ube3a*$^{STOP/p+}$*::Gad2-Cre* littermates, on the other hand, proved to be refractory to audiogenic seizure induction, similar to *Control* (Figure 5B). In contrast, consistent with our flurothyl-induced seizure results, we found that 129S2/SvPasCrl *Ube3a*$^{FLOX/p+}$*::Gad2-Cre* mice exhibit audiogenic seizures much more frequently than *Control* littermates and with a far greater likelihood of progressing from wild running to a severe, tonic-clonic episode (Figure 5C). Surprisingly, post-weaning lethality approached 15% in *Ube3a*$^{FLOX/p+}$*::Gad2-Cre* mice and was associated with observations of spontaneous seizures (Figure 5D), whereas we observed no evidence of postnatal lethality associated with spontaneous seizures in *Ube3a*$^{STOP/p+}$ mice. Collectively, these findings provide compelling evidence that GABAergic, but not glutamatergic, *Ube3a* loss enhances seizure susceptibility. Notably, seizures due to GABAergic *Ube3a* loss alone are more severe than those observed in AS mice with loss of *Ube3a* in both GABAergic and glutamatergic neurons (Table 1).

GABAergic, but Not Glutamatergic, *Ube3a* Loss Mediates AS-like EEG Abnormalities

If GABAergic *Ube3a* loss drives seizure susceptibility in AS, then it might also underlie AS-like EEG abnormalities, including rhythmic, high-amplitude activity in the delta and theta bands (Thibert et al., 2013). To investigate this possibility, we recorded resting-state local field potentials (LFPs) (analogous to intracortical EEG) (Buzsáki et al., 2012) in awake head-fixed mice viewing a gray screen to which they were previously habituated (Figure 6A). We observed a strong trend toward total spectral power being increased in *Ube3a*$^{FLOX/p+}$*::Gad2-Cre* mice relative to *Control* (1–50 Hz power in µV^2: *Control* = 3,195 ± 485.8; *Ube3a*$^{FLOX/p+}$*::Gad2-Cre* = 4,292 ± 293.5; p = 0.07), primarily driven by enhancements in the delta band (Figure 6B). Increased power in other bands including theta (5–10 Hz power in µV^2: *Control* = 755 ± 101.2; *Ube3a*$^{FLOX/p+}$*::Gad2-Cre* = 873 ± 46.8; p = 0.3) and gamma (30–50 Hz power in µV^2: *Control* = 90 ± 9.8; *Ube3a*$^{FLOX/p+}$*::Gad2-Cre* = 101 ± 6; p = 0.37) did not reach statistical significance. Total neocortical power was similarly elevated in *Ube3a*$^{STOP/p+}$ mice (Figure 6C), again largely through delta, with marginal power enhancement in other bands. However, LFP power in *Ube3a*$^{STOP/p+}$*::Gad2-Cre* mice, which model glutamatergic *Ube3a* loss, was normal (Figure 6C); total (1–50 Hz power in µV^2: *Control* = 3,067 ± 252.7; *Ube3a*$^{STOP/p+}$ = 4,255 ± 529.4; *Ube3a*$^{STOP/p+}$*::Gad2-Cre* = 2,755 ± 391.5; p = 0.03), theta (5–10 Hz power in µV^2: *Control* = 733 ± 53.8; *Ube3a*$^{STOP/p+}$ = 879 ± 68.1; *Ube3a*$^{STOP/p+}$*::Gad2-Cre* = 647 ± 92.5; p = 0.11) and gamma (30–50 Hz power in µV^2: *Control* = 105 ± 10.7; *Ube3a*$^{STOP/p+}$ = 127 ± 13.4; *Ube3a*$^{STOP/p+}$*::Gad2-Cre* = 91 ± 13.3; p = 0.16) power was equivalent between *Control* and *Ube3a*$^{STOP/p+}$*::Gad2-Cre* mice. We therefore conclude that GABAergic, but not glutamatergic, *Ube3a* loss yields AS-like enhancements in EEG delta power (Table 1).

GABAergic *Ube3a* Loss Phenocopies Presynaptic CCV Accumulations in AS Mice

We previously linked deficits in inhibitory synaptic recovery in *Ube3a*$^{m-/p+}$ mice to an aberrant accumulation of CCVs at GABAergic synapses (Wallace et al., 2012). This correlation suggests that maternal *Ube3a* loss may cause defective vesicle cycling, which fails to adequately restore presynaptic vesicle

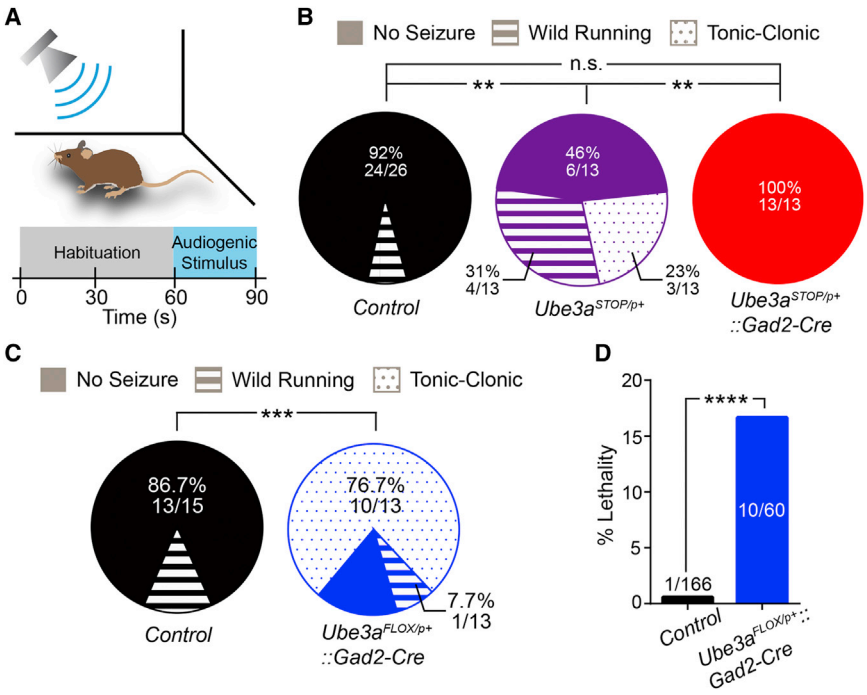

Figure 5. GABAergic, but Not Glutamatergic, *Ube3a* Loss Enhances Audiogenic Seizure Susceptibility in AS Model Mice

(A) Schematic of audiogenic seizure protocol.

(B) Quantification of audiogenic seizure susceptibility in *Control* (n = 26), *Ube3a*$^{STOP/p+}$ (n = 13), and *Ube3a*$^{STOP/p+}$*::Gad2-Cre* (n = 13) mice at ~P80.

(C) Quantification of audiogenic seizure susceptibility (*Control* n = 15; *Ube3a*$^{FLOX/p+}$*::Gad2-Cre* n = 13).

(D) Post-weaning (P21–P90) lethality in *Control* and *Ube3a*$^{FLOX/p+}$*::Gad2-Cre* mice. Data represent mean ± SEM. **p ≤ 0.01; ***p ≤ 0.001; ****p ≤ 0.0001.

pools following bouts of high-frequency release (Cremona et al., 1999; Luthi et al., 2001; Milosevic et al., 2011). However, GABAergic synaptic depletion is normal in *Ube3a*$^{FLOX/p+}$*::Gad2-Cre* mice (Figure 1E), leading us to question whether GABAergic *Ube3a* loss would lead to aberrant presynaptic CCVs. First, we verified that pan-cerebral deletion of the maternal *Ube3a*^{FLOX} allele results in the CCV phenotype, finding that CCVs were increased at dendritic and somatic GABAergic synapses in *Ube3a*$^{FLOX/p+}$*::Nestin-Cre* mice compared to *Control* (Figures S7A–S7C). We also found that CCVs accumulate at glutamatergic synapses in these mice (Figures S7A and S7D), a departure from what we had previously observed in *Ube3a*$^{m-/p+}$ mice, where CCV increases at glutamatergic synapses did not reach statistical significance (Table 1). Next, we tested the effect of GABAergic *Ube3a* deletion on the CCV phenotype, comparing *Ube3a*$^{FLOX/p+}$*::Gad2-Cre* mice with littermate *Controls*. *Ube3a*$^{FLOX/p+}$*::Gad2-Cre* mice did in fact exhibit excessive CCVs at GABAergic presynaptic terminals that synapsed onto the dendrites (Figure 7A$_3$) and somata (Figure 7A$_4$) of glutamatergic neurons in L2/3. Furthermore, we observed excessive CCVs at asymmetric glutamatergic synapses made onto dendritic spines in L2/3 (Figure 7A$_5$). Other presynaptic measures including terminal area (Figures S8A1, S8B1, and S8C1), mitochondrial area (Figures S8A2, S8B2, and S8C2), and the density of synaptic vesicles (Figures S8A3, S8B3, and S8C3) were largely normal. Thus, GABAergic *Ube3a* loss phenocopies the presynaptic CCV abnormalities in AS mice, despite leaving recovery from GABAergic synaptic depletion intact (Figure 1E).

Excessive CCV accumulation also proved to be a feature of both GABAergic and glutamatergic L2/3 synapses in *Ube3a*$^{STOP/p+}$ mice (Figure 7B). To determine if glutamatergic *Ube3a* loss would affect presynaptic CCVs, we compared *Ube3a*$^{STOP/p+}$*::Gad2-Cre* mice to both *Ube3a*$^{STOP/p+}$ and *Control* littermates. We found that *Ube3a*$^{STOP/p+}$*::Gad2-Cre* and *Control* mice were statistically equivalent on measures of CCV density at GABAergic and glutamatergic L2/3 synapses (Figure 7B), indicating that glutamatergic *Ube3a* loss does not contribute to this phenotype in AS mice. Presynaptic measures of terminal area, mitochondrial area, and synaptic vesicle density were similar across the three genotypic groups (Figures S8D–S8F). Importantly, glutamatergic CCV accumulations in *Ube3a*$^{STOP/p+}$ mice occurred in the absence of deficits in glutamatergic synaptic depletion (Figure S5E), providing yet another example of phenotypic dissociation between presynaptic CCVs and the capacity for recovery from synaptic depletion.

DISCUSSION

This work constitutes the first investigation of neuron-type-specific contributions to the pathogenesis of circuit hyperexcitability in AS. We show that GABAergic *Ube3a* deletion produces AS-like enhancements in EEG delta power, enhances seizure susceptibility and severity, and results in aberrant L2/3 presynaptic CCV accumulations. In contrast, glutamatergic *Ube3a* loss impairs the receipt of tonic GABAergic inhibition by L2/3 pyramidal neurons but does not lead to EEG abnormalities or confer vulnerability to seizures.

Our present results demonstrate that GABAergic *Ube3a* loss leads to EEG abnormalities and seizures without producing any of the defects in GABAergic inhibition that we previously observed in L2/3 neocortex in AS mice, which lack *Ube3a* in nearly all neurons (Wallace et al., 2012). The immediate implication of this surprising finding is that defective GABAergic inhibition onto L2/3 pyramidal neurons is neither a cause nor a consequence of circuit hyperexcitability in AS mice. This is consistent with a recent study indicating that EEG abnormalities and seizures occur by P30 in AS mice (Mandel-Brehm et al., 2015), prior to the emergence of mIPSC and eIPSC deficits onto L2/3 pyramidal neurons (Wallace et al., 2012).

Intriguingly, GABAergic *Ube3a* deletion produces atypical accumulations of CCVs in presynaptic terminals (Figures 7A3 and

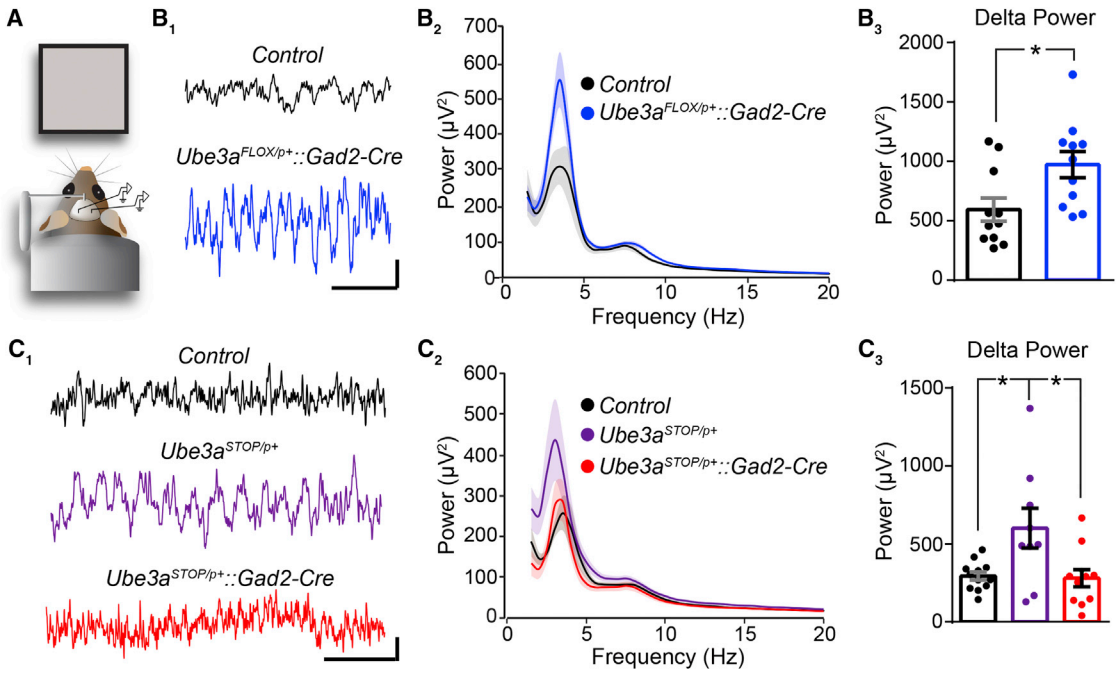

Figure 6. GABAergic *Ube3a* Loss Selectively Enhances LFP Spectral Power in the Delta Band

(A) Schematized configuration for LFP recordings in non-anesthetized mice.

(B) Sample V1 LFP recordings ([B_1], scale bar: 100 μV, 1 s) and quantification of average spectral power (B_2) from *Control* (n = 11) and *Ube3a*$^{FLOX/p+}$*::Gad2-Cre* (n = 11) mice at ~P100. (B_3) Quantification of the region (3 to 4 Hz) encompassing the largest genotypic difference in power within the delta band.

(C) Sample V1 LFP recordings ([C_1], scale bar: 100 μV, 1 s) and quantification of average spectral power (C_2) from from *Control* (n = 12), *Ube3a*$^{STOP/p+}$ (n = 9), and *Ube3a*$^{STOP/p+}$*::Gad2-Cre* (n = 11) mice at ~P100. (C_3) Quantification of the region (2 to 3 Hz) encompassing the largest genotypic difference in power within the delta band. Data represent mean ± SEM. *p ≤ 0.05.

7A4), despite failing to yield deficits in GABAergic synaptic recovery following high-frequency stimulation. Increased presynaptic CCVs are a hallmark of deficient clathrin-mediated endocytosis (Cremona et al., 1999; Luthi et al., 2001; Milosevic et al., 2011), though they could also possibly reflect compensation for impairments in clathrin-independent modes of synaptic vesicle recycling (Daly et al., 2000). Regardless of the underlying cause, accumulations of clathrin-coated endocytic profiles in the synapse typically predict electrophysiological impairments in synaptic depletion and recovery, especially within GABAergic interneurons that display high-frequency firing (Cremona et al., 1999; Luthi et al., 2001; Hayashi et al., 2008). Our electrical stimulation parameters might not have been optimized to reveal deficiencies in synaptic vesicle recycling, perhaps explaining the dissociation between this phenotype and GABAergic presynaptic CCV accumulations. More puzzling is the fact that selective GABAergic *Ube3a* loss led to CCV accumulations at glutamatergic synapses (Figure 7A5); unless *Ube3a* loss in GABAergic neurons triggers cell-nonautonomous defects in synaptic vesicle cycling, we would expect CCV phenotypes to be confined to GABAergic terminals. The parsimonious explanation is that CCV accumulations provide a readout of circuit hyperexcitability owed to GABAergic *Ube3a* loss, signaling the recent history of high-frequency activity at both GABAergic and glutamatergic presynaptic terminals. It remains to be elucidated how *Ube3a* loss impairs GABAergic synaptic recovery in AS mice, but our data implicate a mechanism requiring loss of *Ube3a* in both glutamatergic and GABAergic neurons (Figures 1E3 and 2D3).

Implications of Defective Tonic GABAergic Inhibition in AS Mice

Here we show that glutamatergic *Ube3a* loss impairs the receipt of tonic GABAergic inhibition by L2/3 pyramidal neurons in the absence of EEG abnormalities and seizures (Figures 3G, 5B, and 6C), indicating a lack of relevance to the pathogenesis of hyperexcitability in AS. Considering the apparent cell-autonomous nature of this defect, it is reasonable to speculate that tonic GABAergic tone onto GABAergic neurons is also diminished in AS. However, such a deficit is equally unlikely to factor in the pathogenesis of hyperexcitability; GABAergic neuron-specific deletion of δ-$GABA_A$Rs actually enhances phasic inhibition, thereby suppressing hippocampal network excitability and seizure susceptibility (Lee and Maguire, 2013). Nevertheless, decreases in tonic GABAergic neurotransmission have the potential to alter network dynamics throughout the brain (Brickley and Mody, 2012; Lee and Maguire, 2014) and may contribute to the manifestation of AS phenotypes besides epilepsy. For example, tonic inhibitory deficits onto cerebellar granule cells in AS mice are linked to impaired locomotion, which is amenable to rescue by the δ-$GABA_A$R superagonist THIP (Gaboxadol) (Egawa et al., 2012). It has since been shown that cerebellar deficits consequent to the loss of tonic GABAergic inhibition onto

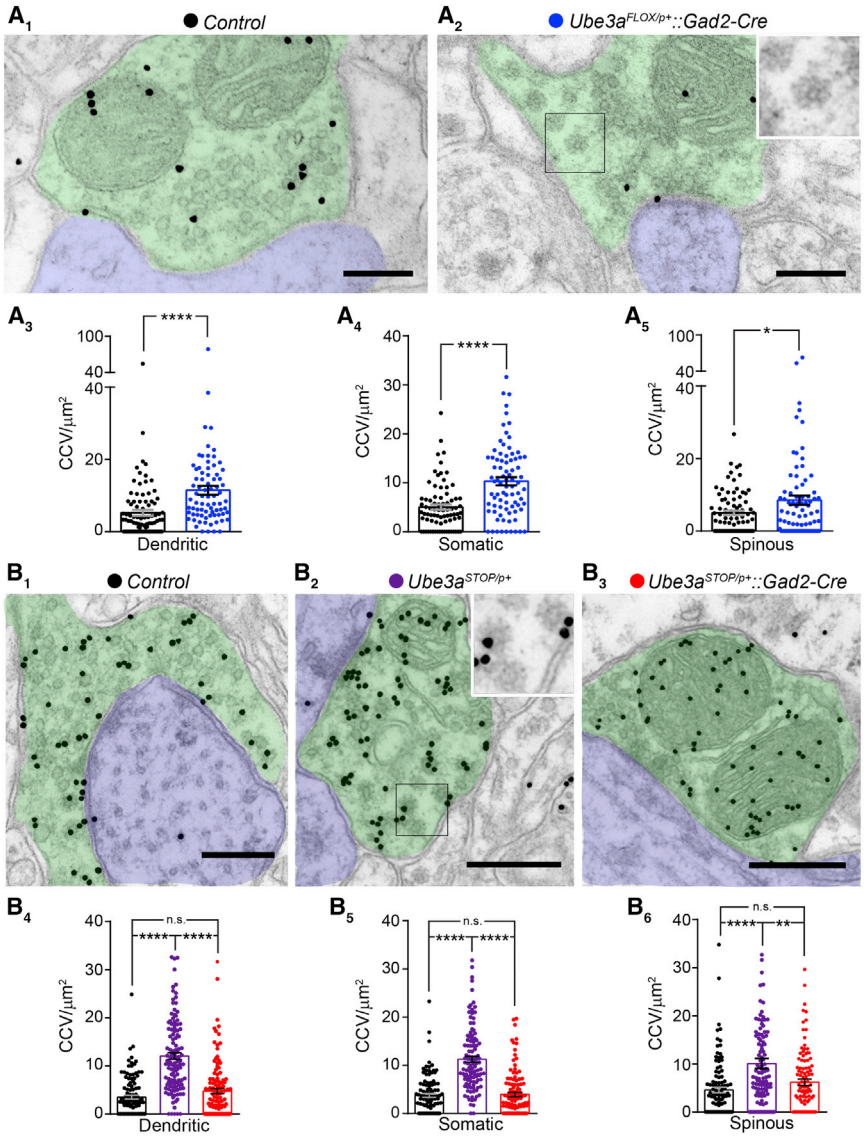

Figure 7. GABAergic *Ube3a* Loss Underlies Presynaptic CCV Accumulation at Both GABAergic and Glutamatergic Synapses

(A) Electron micrographs of dendritic inhibitory synapses stained for GABA in *Control* (A_1) and *Ube3a*$^{FLOX/p+}$*::Gad2-Cre* (A_2) mice at ~P80. Green denotes GABAergic axon terminal, blue denotes dendrite, inset highlights clathrin-coated vesicles (CCVs) (scale bar: 200 nm). Average CCV densities at dendritic GABAergic synapses ([A_3], *Control* n = 89 synapses from 3 mice; *Ube3a*$^{FLOX/p+}$*::Gad2-Cre* n = 77 synapses from three mice), somatic GABAergic synapses ([A_4], *Control* n = 78 synapses from three mice; *Ube3a*$^{FLOX/p+}$*::Gad2-Cre* n = 81 synapses from three mice), and spinous glutamatergic synapses ([A_5], *Control* n = 82 synapses from three mice; *Ube3a*$^{FLOX/p+}$*::Gad2-Cre* n = 80 synapses from three mice).

(B) Electron micrographs of dendritic inhibitory synapses stained for GABA in *Control* (B_1), *Ube3a*$^{STOP/p+}$ (B_2), and *Ube3a*$^{STOP/p+}$*::Gad2-Cre* (B_3) mice at ~P80. Green denotes GABAergic axon terminal, blue denotes dendrite, inset highlights CCVs (scale bar: 400 nm). Average CCV densities at dendritic GABAergic synapses ([B_4], *Control* n = 110 synapses from three mice; *Ube3a*$^{STOP/p+}$ n = 119 synapses from three mice; *Ube3a*$^{STOP/p+}$*::Gad2-Cre* n = 115 synapses from three mice), somatic GABAergic synapses ([B_5], *Control* n = 103 synapses from three mice; *Ube3a*$^{STOP/p+}$ n = 114 synapses from three mice; *Ube3a*$^{STOP/p+}$*::Gad2-Cre* n = 110 synapses from three mice), and spinous glutamatergic synapses (B_6, *Control* n = 108 synapses from three mice; *Ube3a*$^{STOP/p+}$ n = 113 synapses from three mice; *Ube3a*$^{STOP/p+}$*::Gad2-Cre* n = 113 synapses from three mice). Data represent mean ± SEM. *p ≤ 0.05; **p ≤ 0.01; ****p ≤ 0.0001.

cerebellar granule cells are clearly dissociable from locomotor defects (Bruinsma et al., 2015), suggesting that any therapeutic benefit of THIP for gross motor dysfunction works through the enhancement of tonic GABAergic inhibition in extracerebellar circuits. Together with our present findings, these studies underscore the need for further preclinical elucidation of a complex relationship between deficits in tonic inhibition and AS-like phenotypes; such knowledge will be essential to inform future clinical trials of THIP administration in AS patients—especially with regard to the selection of appropriate clinical endpoints.

Insights into Circuit-Level Consequences of GABAergic *Ube3a* Loss

What are the physiological mechanisms by which GABAergic *Ube3a* loss contributes to circuit imbalance? We previously found that neocortical fast-spiking interneurons receive normal excitatory synaptic drive and display appropriate intrinsic excitability in the absence of *Ube3a* (Wallace et al., 2012), and our present studies indicate that a loss of GABAergic inhibition onto L2/3 pyramidal neurons is not involved in mediating circuit hyperexcitability (Figures 1, 4, 5, 6, and 7). These findings highlight the importance of moving beyond the L2/3 neocortical microcircuit to elucidate the physiological consequences of GABAergic *Ube3a* loss. While this is a vast parameter space, potentially involving numerous GABAergic neuron populations, our EEG findings point to a major role for the thalamic reticular nucleus (TRN). GABAergic TRN neurons directly regulate the oscillatory activity of thalamocortical circuits and, when activated, are capable of mediating selective enhancements of neocortical EEG power in the delta band (Zhang et al., 2009; Lewis et al., 2015)—the same power band in which we observed the majority of EEG power enhancement following GABAergic *Ube3a* loss. Indeed, pathological synchrony of TRN neurons has been implicated in the generation of delta frequency spike-wave oscillations and atypical absence seizures (Steriade, 2005; Huguenard and McCormick, 2007), both of which are commonly observed in AS (Vendrame et al., 2012; Thibert et al., 2013). High-amplitude

theta rhythmicity (4–6 Hz) with spiking is another common background EEG abnormality in AS (Thibert et al., 2013). Although this theta abnormality is most prominent in occipital regions, it seems to disappear by adolescence (Laan et al., 1997), perhaps explaining why we did not record significant enhancements in theta power in adult *Ube3a*$^{STOP/p+}$ or *Ube3a*$^{FLOX/p+}$*::Gad2-Cre* mice, despite recording from V1 (Figure 6). Future work in AS models should focus on factors known to affect TRN neuron excitability and synchrony—including relative levels of excitatory and inhibitory synaptic drive, the integrity of gap junctions (Proulx et al., 2006; Lee et al., 2014), the expression of T-type calcium channels (Tsakiridou et al., 1995; Zhang et al., 2009), and cholinergic input (McCormick and Prince, 1986; Sun et al., 2013). However, intracortical GABAergic mechanisms that underlie pathological spike-wave discharges also remain of interest, especially those that engage disinhibitory circuitry (Pi et al., 2013; Hall et al., 2015).

Numerous GABAergic circuits outside the thalamus and cortex could also contribute to the enhancements in seizure susceptibility that we observed following GABAergic *Ube3a* loss. This might even be expected, considering the variety of seizure types known to occur in individuals with AS (Galván-Manso et al., 2005; Thibert et al., 2013). GABAergic circuits in the temporal lobe, hypothalamus, and striatum are all potentially of interest, but they have yet to be formally investigated. We have also yet to explore the possibility that GABAergic *Ube3a* loss mediates AS-like phenotypes other than EEG abnormalities and seizures. Recent findings suggest that GABAergic *Mecp2* loss precipitates the majority of Rett syndrome-like phenotypes in mice (Chao et al., 2010; Ito-Ishida et al., 2015). Considering the high degree of phenotypic overlap between AS and Rett syndrome (Jedele, 2007; Tan et al., 2014), this might foreshadow a similarly broad penetrance of AS-like phenotypes following GABAergic *Ube3a* loss. On the other hand, there is clearly divergence in the developmental mechanisms underlying AS and Rett syndrome, as indicated by studies modeling the temporal requirements for *Ube3a* and *Mecp2* gene reinstatement therapy, respectively (Guy et al., 2007; Silva-Santos et al., 2015).

Neuron-Type-Specific Strategies for the Treatment of Circuit Hyperexcitability in AS

Ube3a$^{STOP/p+}$*::Gad2-Cre* mice dually serve to model the effects of glutamatergic *Ube3a* loss as well as the therapeutic value of GABAergic *Ube3a* reinstatement. The lack of EEG abnormalities, seizures, and associated CCV accumulations in this line (Figures 5, 6, and 7) demonstrates the promise that GABAergic neuron-specific treatments hold for the treatment of hyperexcitability phenotypes in AS. However, this promise has its limits. Modeling of pan-cellular *Ube3a* reinstatement in *Ube3a*$^{STOP/p+}$ mice predicts closure of a critical period for the amelioration of hyperexcitability phenotypes very early during postnatal development (Silva-Santos et al., 2015). Furthermore, GABAergic neuron-specific therapeutic approaches in AS are unlikely to involve the reinstatement of *UBE3A* expression. The only tractable target for the reinstatement of *UBE3A* expression in individuals with AS is the paternal *UBE3A* allele. Paternal *UBE3A* is intact, but epigenetically silenced in *cis* by a long non-coding RNA that includes a 3′ *UBE3A-antisense* (*UBE3A-ATS*) sequence (Rougeulle et al., 1998; Martins-Taylor et al., 2014). Thus far, successful preclinical efforts to unsilence paternal *Ube3a* have depended directly (Meng et al., 2015) or indirectly (Huang et al., 2012) on the down-regulation of *Ube3a-ATS*, which appears to be uniformly expressed by glutamatergic and GABAergic neurons. Therefore, signaling pathways that functionally intersect with UBE3A are more likely to provide neuron-type-specific targets for the development of AS therapeutics.

As a proof of concept, genetic normalization of calcium/calmodulin-dependent kinase type 2-α subunit (CaMKII-α) inhibitory hyperphosphorylation—a signaling deficit which decreases CaMKII enzymatic activity in *Ube3a*$^{m-/p+}$ mice (Weeber et al., 2003)—rescues seizure phenotypes (van Woerden et al., 2007). Moreover, genetic reduction of the immediate-early gene, *Arc* (*Arc*$^{+/-}$), whose expression UBE3A may regulate either transcriptionally or posttranslationally through ubiquitination (Greer et al., 2010; Kühnle et al., 2013), normalizes EEG and abnormal responses to audiogenic stimuli in *Ube3a*$^{m-/p+}$ mice (Mandel-Brehm et al., 2015). *Arc* expression is preferentially induced in CaMKII-α-expressing neurons in response to convulsive seizures (Vazdarjanova et al., 2006), indicating that the restoration of circuit balance in *Ube3a*$^{m-/p+}$*::Arc*$^{+/-}$ mice may also be mediated by these cells. This poses a puzzle, however, considering our compelling evidence that GABAergic, but not glutamatergic, *Ube3a* loss drives the pathogenesis of hyperexcitability; in most brain regions including the cortex and hippocampus, CaMKII-α expression is restricted to glutamatergic neurons (Benson et al., 1992). An exception is the striatum in which CaMKII-α activity and *Arc* expression are readily induced within GABAergic spiny projection neurons in response to a variety of stimuli (Tan et al., 2000; Choe and Wang, 2002; Vazdarjanova et al., 2006; Anderson et al., 2008). GABAergic spiny projection neurons may thus be a nexus for seizure susceptibility or seizure resistance as mediated by loss or reinstatement of *Ube3a*, respectively. Alternatively, normalization of CaMKII-α and ARC function may work intrinsically through glutamatergic circuits to dampen their excitability and restore circuit balance, countering inhibitory deficits mediated by GABAergic *Ube3a* loss.

In summary, the present data compel us to revisit, reevaluate, and refine our previous hypotheses regarding the pathogenesis of circuit hyperexcitability in AS. We now appreciate that GABAergic *UBE3A* loss is likely to be the principal pathogenic factor underlying circuit hyperexcitability in the disorder; accordingly, the restoration of GABAergic neuronal function represents the most direct therapeutic strategy for the prevention or reversal of EEG abnormalities and seizures, provided the intervention occurs sufficiently early in development. This conceptual advance should help to focus future studies of the molecular mechanisms working both upstream and downstream of UBE3A within GABAergic neurons, perhaps yielding novel, actionable therapeutic targets.

EXPERIMENTAL PROCEDURES

See Supplemental Experimental Procedures for experimental details relating to mouse lines, AAV-Cre injections, electrophysiology, flurothyl-induced seizure assays, audiogenic seizure assays, qRT-PCR, western blotting, immunohistochemistry, and statistical analyses.

Animals

We raised all mice on a 12:12 light:dark cycle with ad libitum access to food and water. We used both male and female littermates at equivalent genotypic ratios and in strict compliance with animal protocols approved by the Institutional Animal Care and Use Committees of the University of North Carolina at Chapel Hill.

Electrophysiology

Whole-Cell Voltage-Clamp Recordings

We placed coronal slices containing V1 (see Supplemental Experimental Procedures) in a submersion chamber maintained at 30°C and perfused at 2 ml/min with oxygenated ACSF (in mM: 124 NaCl, 3 KCl, 1.25 NaH_2PO_4, 26 $NaHCO_3$, 1 $MgCl_2$, 2 $CaCl_2$, and 20 dextrose). We pulled patch pipettes from thick-walled borosilicate glass using a P2000 laser puller (Sutter Instruments). Open tip resistances were between 2–5 MΩ when pipettes were filled with the internal solution containing (in mM) 100 $CsCH_3SO_3$, 15 CsCl, 2.5 $MgCl_2$, 5 QX-314-Cl, 5 tetra-Cs-BAPTA, 10 HEPES, 4 Mg-ATP, 0.3 Na-GTP, and 0.025 Alexa-594, with pH adjusted to 7.25 and osmolarity adjusted to ~295 mOsm with sucrose.

We visually targeted L2/3 pyramidal neurons for recording using an Axio Examiner microscope (Zeiss, Germany) equipped with infrared differential interference contrast and epifluorescence optics. For successfully patched neurons, we achieved pipette seal resistances >1 GΩ, minimizing pipette capacitive transients prior to breakthrough. We performed voltage-clamp recordings in the whole-cell configuration using a Multiclamp 700B amplifier (Molecular Devices) with 10 kHz digitization and a 2 kHz low-pass Bessel filter. We acquired and analyzed data using pCLAMP 10 software (Molecular Devices, RRID:SCR_011323). We monitored changes in series and input resistance throughout each experiment by giving test step of −5 mV every 30 s and measuring the resultant amplitude of the capacitive current. We discarded neurons if series resistance surpassed 25 MΩ or if series resistance or input resistance changed by >25% during the course of an experiment. We confirmed L2/3 pyramidal neuronal identity by analyzing characteristic membrane properties (Table S1) and the presence of dendritic spines and prominent apical dendrites visualized with Alexa-594 dye.

In Vivo LFP Recordings

We backcrossed mice used for LFP and audiogenic seizure experiments (see Supplemental Experimental Procedures) six to seven generations onto the 129S2/SvPasCrl background, which is permissive for hyperexcitability phenotypes. For surgeries, we anesthetized adult mice (P75–118 on day 1 of recording) via intraperitoneal injections of ketamine (40 mg/kg) and xylazine (10 mg/kg), with 0.25% bupivacaine injected under the scalp for local analgesia. We then bilaterally implanted tungsten microelectrodes (FHC) in layer 4 of V1 (3.2–3.3 mm lateral to Lambda, 0.47 mm depth) and placed a silver wire in prefrontal cortex as a reference electrode. In order to enable head fixation during recordings, we attached a steel headpost to the skull anterior to bregma. We used dental cement to secure all elements in place and create a protective head cap.

We allowed mice to recover for at least 2 days following surgery before habituating them to the recording apparatus over 2 consecutive days. We acquired LFP data over the next 3 consecutive days. We head-fixed mice during all recording sessions (both habituation and LFP), orienting them toward a full-field gray screen for 15 min in a dark, quiet environment. We amplified LFP recordings 1,000× using single-channel amplifiers (Grass Technologies) with 0.1 Hz low-pass and 100 Hz high-pass filtration preceding acquisition and digitization at 4 kHz using Spike2 software (CED Ltd., RRID: SCR_000903). We analyzed spectral power using a fast Fourier transform resulting in bin sizes of 0.5 Hz. Prior to analysis, we manually excluded rarely occurring electrical artifacts corresponding to mouse movement. For each animal, we averaged power spectra from both hemispheres across all 3 days of recording.

Statistics

We performed all experiments and analyses blind to genotype. We performed all statistical analyses using GraphPad Prism 6 software (GraphPad Software Inc., RRID: SCR_002798).

SUPPLEMENTAL INFORMATION

Supplemental Information includes eight figures, one table, and Supplemental Experimental Procedures and can be found with this article online at http://dx.doi.org/10.1016/j.neuron.2016.02.040.

AUTHOR CONTRIBUTIONS

M.C.J. generated and molecularly characterized *Ube3a*^{FLOX} mice and designed and performed light microscopy, whole-cell electrophysiology, and behavioral seizure experiments. M.L.W. designed and performed whole-cell electrophysiology and audiogenic seizure experiments. M.S.S. designed and performed in vivo electrophysiology experiments. A.C.B. designed and performed electron microscopy experiments. B.G. designed and performed flurothyl seizure experiments. G.M.v.W. advised on *Ube3a*$^{STOP/p+}$ experiments. I.F.K. performed qRT-PCR experiments. J.E.H. performed light microscopic analyses. M.J.Z. advised on qRT-PCR experiments. Y.E. advised on *Ube3a*$^{STOP/p+}$ experiments. R.J.W. designed experiments. B.D.P. designed experiments. M.C.J., M.L.W., R.J.W, and B.P. wrote the manuscript, which was edited by all co-authors.

CONFLICTS OF INTEREST

The authors declare that they have no competing financial interests.

ACKNOWLEDGMENTS

We thank Rylan Larsen and Janet Berrios for critical readings of the manuscript, Hyojin Kim for maintaining animal colonies, Kristen Phend for histological support, Dale Cowley and George Altshuller at the UNC Animal Models Core, William D. Snider for providing AAV-Cre virus, and Klaus-Armin Nave for providing *NEX-Cre* mice. This work was supported by NRSA fellowships 5F32NS077686 (to M.C.J.) and 1F31NS077847 (to M.L.W.), an NRSA institutional postdoctoral training grant T32-HD40127 (to M.S.S.), the Angelman Syndrome Foundation's Joseph E. Wagstaff fellowship (to I.F.K.), Angelman Syndrome Foundation grants (to Y.E. and B.D.P.), Simons Foundation SFARI Awards 274426 (to B.D.P.) and 275234 (to Y.E.), a Netherlands Organization for Scientific Research grant-ZonNMW (to Y.E.), a Hersenstichting grant (to G.M.v.W.), NIMH 5RO1MHO93372 (to M.J.Z. and B.D.P.), NINDS 5RO1NS039444 (to R.J.W.), and NINDS 1RO1NS085093 (to B.D.P.). Confocal imaging was supported by NINDS Center Grant P30 NS045892 and NICHD Center Grant P30 HD03110. NIH grants to Velocigene at Regeneron Inc. (U01HG004085), the CSD Consortium (U01HG004080), and the KOMP Repository at UC Davis and CHORI (U42RR024244) funded the generation, curation, and distribution of the targeting vector used to produce *Ube3a*^{FLOX} mice.

Received: March 19, 2015
Revised: January 17, 2016
Accepted: February 24, 2016
Published: March 24, 2016

REFERENCES

Anderson, S.M., Famous, K.R., Sadri-Vakili, G., Kumaresan, V., Schmidt, H.D., Bass, C.E., Terwilliger, E.F., Cha, J.H., and Pierce, R.C. (2008). CaMKII: a biochemical bridge linking accumbens dopamine and glutamate systems in cocaine seeking. Nat. Neurosci. *11*, 344–353.

Benson, D.L., Isackson, P.J., Gall, C.M., and Jones, E.G. (1992). Contrasting patterns in the localization of glutamic acid decarboxylase and Ca2+/calmodulin protein kinase gene expression in the rat central nervous system. Neuroscience *46*, 825–849.

Brickley, S.G., and Mody, I. (2012). Extrasynaptic GABA(A) receptors: their function in the CNS and implications for disease. Neuron *73*, 23–34.

Bruinsma, C.F., Schonewille, M., Gao, Z., Aronica, E.M., Judson, M.C., Philpot, B.D., Hoebeek, F.E., van Woerden, G.M., De Zeeuw, C.I., and

Elgersma, Y. (2015). Dissociation of locomotor and cerebellar deficits in a murine Angelman syndrome model. J. Clin. Invest. *125*, 4305–4315.

Buzsáki, G., Anastassiou, C.A., and Koch, C. (2012). The origin of extracellular fields and currents–EEG, ECoG, LFP and spikes. Nat. Rev. Neurosci. *13*, 407–420.

Chao, H.T., Chen, H., Samaco, R.C., Xue, M., Chahrour, M., Yoo, J., Neul, J.L., Gong, S., Lu, H.C., Heintz, N., et al. (2010). Dysfunction in GABA signalling mediates autism-like stereotypies and Rett syndrome phenotypes. Nature *468*, 263–269.

Choe, E.S., and Wang, J.Q. (2002). CaMKII regulates amphetamine-induced ERK1/2 phosphorylation in striatal neurons. Neuroreport *13*, 1013–1016.

Cooper, E.M., Hudson, A.W., Amos, J., Wagstaff, J., and Howley, P.M. (2004). Biochemical analysis of Angelman syndrome-associated mutations in the E3 ubiquitin ligase E6-associated protein. J. Biol. Chem. *279*, 41208–41217.

Coulter, D.A., and Carlson, G.C. (2007). Functional regulation of the dentate gyrus by GABA-mediated inhibition. Prog. Brain Res. *163*, 235–243.

Cremona, O., Di Paolo, G., Wenk, M.R., Lüthi, A., Kim, W.T., Takei, K., Daniell, L., Nemoto, Y., Shears, S.B., Flavell, R.A., et al. (1999). Essential role of phosphoinositide metabolism in synaptic vesicle recycling. Cell *99*, 179–188.

Daly, C., Sugimori, M., Moreira, J.E., Ziff, E.B., and Llinás, R. (2000). Synaptophysin regulates clathrin-independent endocytosis of synaptic vesicles. Proc. Natl. Acad. Sci. USA *97*, 6120–6125.

Dibbens, L.M., Feng, H.J., Richards, M.C., Harkin, L.A., Hodgson, B.L., Scott, D., Jenkins, M., Petrou, S., Sutherland, G.R., Scheffer, I.E., et al. (2004). GABRD encoding a protein for extra- or peri-synaptic GABAA receptors is a susceptibility locus for generalized epilepsies. Hum. Mol. Genet. *13*, 1315–1319.

Egawa, K., Kitagawa, K., Inoue, K., Takayama, M., Takayama, C., Saitoh, S., Kishino, T., Kitagawa, M., and Fukuda, A. (2012). Decreased tonic inhibition in cerebellar granule cells causes motor dysfunction in a mouse model of Angelman syndrome. Sci. Transl. Med. *4*, 163ra157.

Galván-Manso, M., Campistol, J., Conill, J., and Sanmartí, F.X. (2005). Analysis of the characteristics of epilepsy in 37 patients with the molecular diagnosis of Angelman syndrome. Epileptic Disord. *7*, 19–25.

Goebbels, S., Bormuth, I., Bode, U., Hermanson, O., Schwab, M.H., and Nave, K.A. (2006). Genetic targeting of principal neurons in neocortex and hippocampus of NEX-Cre mice. Genesis *44*, 611–621.

Greer, P.L., Hanayama, R., Bloodgood, B.L., Mardinly, A.R., Lipton, D.M., Flavell, S.W., Kim, T.K., Griffith, E.C., Waldon, Z., Maehr, R., et al. (2010). The Angelman Syndrome protein Ube3A regulates synapse development by ubiquitinating arc. Cell *140*, 704–716.

Guy, J., Gan, J., Selfridge, J., Cobb, S., and Bird, A. (2007). Reversal of neurological defects in a mouse model of Rett syndrome. Science *315*, 1143–1147.

Hall, S., Hunt, M., Simon, A., Cunnington, L.G., Carracedo, L.M., Schofield, I.S., Forsyth, R., Traub, R.D., and Whittington, M.A. (2015). Unbalanced Peptidergic Inhibition in Superficial Neocortex Underlies Spike and Wave Seizure Activity. J. Neurosci. *35*, 9302–9314.

Hayashi, M., Raimondi, A., O'Toole, E., Paradise, S., Collesi, C., Cremona, O., Ferguson, S.M., and De Camilli, P. (2008). Cell- and stimulus-dependent heterogeneity of synaptic vesicle endocytic recycling mechanisms revealed by studies of dynamin 1-null neurons. Proc. Natl. Acad. Sci. USA *105*, 2175–2180.

Hsu, D. (2007). The dentate gyrus as a filter or gate: a look back and a look ahead. Prog. Brain Res. *163*, 601–613.

Huang, H.S., Allen, J.A., Mabb, A.M., King, I.F., Miriyala, J., Taylor-Blake, B., Sciaky, N., Dutton, J.W., Jr., Lee, H.M., Chen, X., et al. (2012). Topoisomerase inhibitors unsilence the dormant allele of Ube3a in neurons. Nature *481*, 185–189.

Huguenard, J.R., and McCormick, D.A. (2007). Thalamic synchrony and dynamic regulation of global forebrain oscillations. Trends Neurosci. *30*, 350–356.

Ito-Ishida, A., Ure, K., Chen, H., Swann, J.W., and Zoghbi, H.Y. (2015). Loss of MeCP2 in Parvalbumin-and Somatostatin-Expressing Neurons in Mice Leads to Distinct Rett Syndrome-like Phenotypes. Neuron *88*, 651–658.

Jedele, K.B. (2007). The overlapping spectrum of rett and angelman syndromes: a clinical review. Semin. Pediatr. Neurol. *14*, 108–117.

Jiang, Y.H., Armstrong, D., Albrecht, U., Atkins, C.M., Noebels, J.L., Eichele, G., Sweatt, J.D., and Beaudet, A.L. (1998). Mutation of the Angelman ubiquitin ligase in mice causes increased cytoplasmic p53 and deficits of contextual learning and long-term potentiation. Neuron *21*, 799–811.

Judson, M.C., Sosa-Pagan, J.O., Del Cid, W.A., Han, J.E., and Philpot, B.D. (2014). Allelic specificity of Ube3a expression in the mouse brain during postnatal development. J. Comp. Neurol. *522*, 1874–1896.

Kadiyala, S.B., Papandrea, D., Herron, B.J., and Ferland, R.J. (2014). Segregation of seizure traits in C57 black mouse substrains using the repeated-flurothyl model. PLoS ONE *9*, e90506.

Kishino, T., Lalande, M., and Wagstaff, J. (1997). UBE3A/E6-AP mutations cause Angelman syndrome. Nat. Genet. *15*, 70–73.

Krasowski, M.D. (2000). Differential modulatory actions of the volatile convulsant flurothyl and its anesthetic isomer at inhibitory ligand-gated ion channels. Neuropharmacology *39*, 1168–1183.

Kühnle, S., Mothes, B., Matentzoglu, K., and Scheffner, M. (2013). Role of the ubiquitin ligase E6AP/UBE3A in controlling levels of the synaptic protein Arc. Proc. Natl. Acad. Sci. USA *110*, 8888–8893.

Laan, L.A., Renier, W.O., Arts, W.F., Buntinx, I.M., vd Burgt, I.J., Stroink, H., Beuten, J., Zwinderman, K.H., van Dijk, J.G., and Brouwer, O.F. (1997). Evolution of epilepsy and EEG findings in Angelman syndrome. Epilepsia *38*, 195–199.

Lee, V., and Maguire, J. (2013). Impact of inhibitory constraint of interneurons on neuronal excitability. J. Neurophysiol. *110*, 2520–2535.

Lee, V., and Maguire, J. (2014). The impact of tonic GABAA receptor-mediated inhibition on neuronal excitability varies across brain region and cell type. Front. Neural Circuits *8*, 3.

Lee, S.C., Patrick, S.L., Richardson, K.A., and Connors, B.W. (2014). Two functionally distinct networks of gap junction-coupled inhibitory neurons in the thalamic reticular nucleus. J. Neurosci. *34*, 13170–13182.

Lewis, L.D., Voigts, J., Flores, F.J., Schmitt, L.I., Wilson, M.A., Halassa, M.M., and Brown, E.N. (2015). Thalamic reticular nucleus induces fast and local modulation of arousal state. eLife *4*, e08760.

Luthi, A., Di Paolo, G., Cremona, O., Daniell, L., De Camilli, P., and McCormick, D.A. (2001). Synaptojanin 1 contributes to maintaining the stability of GABAergic transmission in primary cultures of cortical neurons. J. Neurosci. *21*, 9101–9111.

Mabb, A.M., and Ehlers, M.D. (2010). Ubiquitination in postsynaptic function and plasticity. Annu. Rev. Cell Dev. Biol. *26*, 179–210.

Mabb, A.M., Judson, M.C., Zylka, M.J., and Philpot, B.D. (2011). Angelman syndrome: insights into genomic imprinting and neurodevelopmental phenotypes. Trends Neurosci. *34*, 293–303.

Maguire, J.L., Stell, B.M., Rafizadeh, M., and Mody, I. (2005). Ovarian cycle-linked changes in GABA(A) receptors mediating tonic inhibition alter seizure susceptibility and anxiety. Nat. Neurosci. *8*, 797–804.

Mandel-Brehm, C., Salogiannis, J., Dhamne, S.C., Rotenberg, A., and Greenberg, M.E. (2015). Seizure-like activity in a juvenile Angelman syndrome mouse model is attenuated by reducing Arc expression. Proc. Natl. Acad. Sci. USA *112*, 5129–5134.

Martins-Taylor, K., Hsiao, J.S., Chen, P.F., Glatt-Deeley, H., De Smith, A.J., Blakemore, A.I., Lalande, M., and Chamberlain, S.J. (2014). Imprinted expression of UBE3A in non-neuronal cells from a Prader-Willi syndrome patient with an atypical deletion. Hum. Mol. Genet. *23*, 2364–2373.

Matsuura, T., Sutcliffe, J.S., Fang, P., Galjaard, R.J., Jiang, Y.H., Benton, C.S., Rommens, J.M., and Beaudet, A.L. (1997). De novo truncating mutations in E6-AP ubiquitin-protein ligase gene (UBE3A) in Angelman syndrome. Nat. Genet. *15*, 74–77.

McCormick, D.A., and Prince, D.A. (1986). Acetylcholine induces burst firing in thalamic reticular neurones by activating a potassium conductance. Nature *319*, 402–405.

Meng, L., Ward, A.J., Chun, S., Bennett, C.F., Beaudet, A.L., and Rigo, F. (2015). Towards a therapy for Angelman syndrome by targeting a long non-coding RNA. Nature *518*, 409–412.

Milosevic, I., Giovedi, S., Lou, X., Raimondi, A., Collesi, C., Shen, H., Paradise, S., O'Toole, E., Ferguson, S., Cremona, O., and De Camilli, P. (2011). Recruitment of endophilin to clathrin-coated pit necks is required for efficient vesicle uncoating after fission. Neuron *72*, 587–601.

Nieto, M., Monuki, E.S., Tang, H., Imitola, J., Haubst, N., Khoury, S.J., Cunningham, J., Gotz, M., and Walsh, C.A. (2004). Expression of Cux-1 and Cux-2 in the subventricular zone and upper layers II-IV of the cerebral cortex. J. Comp. Neurol. *479*, 168–180.

Pi, H.J., Hangya, B., Kvitsiani, D., Sanders, J.I., Huang, Z.J., and Kepecs, A. (2013). Cortical interneurons that specialize in disinhibitory control. Nature *503*, 521–524.

Proulx, E., Leshchenko, Y., Kokarovtseva, L., Khokhotva, V., El-Beheiry, M., Snead, O.C., 3rd, and Perez Velazquez, J.L. (2006). Functional contribution of specific brain areas to absence seizures: role of thalamic gap-junctional coupling. Eur. J. Neurosci. *23*, 489–496.

Pun, R.Y., Rolle, I.J., Lasarge, C.L., Hosford, B.E., Rosen, J.M., Uhl, J.D., Schmeltzer, S.N., Faulkner, C., Bronson, S.L., Murphy, B.L., et al. (2012). Excessive activation of mTOR in postnatally generated granule cells is sufficient to cause epilepsy. Neuron *75*, 1022–1034.

Rotin, D., and Kumar, S. (2009). Physiological functions of the HECT family of ubiquitin ligases. Nat. Rev. Mol. Cell Biol. *10*, 398–409.

Rougeulle, C., Glatt, H., and Lalande, M. (1997). The Angelman syndrome candidate gene, UBE3A/E6-AP, is imprinted in brain. Nat. Genet. *17*, 14–15.

Rougeulle, C., Cardoso, C., Fontés, M., Colleaux, L., and Lalande, M. (1998). An imprinted antisense RNA overlaps UBE3A and a second maternally expressed transcript. Nat. Genet. *19*, 15–16.

Silva-Santos, S., van Woerden, G.M., Bruinsma, C.F., Mientjes, E., Jolfaei, M.A., Distel, B., Kushner, S.A., and Elgersma, Y. (2015). Ube3a reinstatement identifies distinct developmental windows in a murine Angelman syndrome model. J. Clin. Invest. *125*, 2069–2076.

Spigelman, I., Li, Z., Banerjee, P.K., Mihalek, R.M., Homanics, G.E., and Olsen, R.W. (2002). Behavior and physiology of mice lacking the GABAA-receptor delta subunit. Epilepsia *43* (*Suppl 5*), 3–8.

Steriade, M. (2005). Sleep, epilepsy and thalamic reticular inhibitory neurons. Trends Neurosci. *28*, 317–324.

Sun, Y.G., Pita-Almenar, J.D., Wu, C.S., Renger, J.J., Uebele, V.N., Lu, H.C., and Beierlein, M. (2013). Biphasic cholinergic synaptic transmission controls action potential activity in thalamic reticular nucleus neurons. J. Neurosci. *33*, 2048–2059.

Sutcliffe, J.S., Jiang, Y.H., Galijaard, R.J., Matsuura, T., Fang, P., Kubota, T., Christian, S.L., Bressler, J., Cattanach, B., Ledbetter, D.H., and Beaudet, A.L. (1997). The E6-Ap ubiquitin-protein ligase (UBE3A) gene is localized within a narrowed Angelman syndrome critical region. Genome Res. *7*, 368–377.

Tan, A., Moratalla, R., Lyford, G.L., Worley, P., and Graybiel, A.M. (2000). The activity-regulated cytoskeletal-associated protein arc is expressed in different striosome-matrix patterns following exposure to amphetamine and cocaine. J. Neurochem. *74*, 2074–2078.

Tan, W.H., Bird, L.M., Thibert, R.L., and Williams, C.A. (2014). If not Angelman, what is it? A review of Angelman-like syndromes. Am. J. Med. Genet. A. *164A*, 975–992.

Taniguchi, H., He, M., Wu, P., Kim, S., Paik, R., Sugino, K., Kvitsiani, D., Fu, Y., Lu, J., Lin, Y., et al. (2011). A resource of Cre driver lines for genetic targeting of GABAergic neurons in cerebral cortex. Neuron *71*, 995–1013.

Thibert, R.L., Larson, A.M., Hsieh, D.T., Raby, A.R., and Thiele, E.A. (2013). Neurologic manifestations of Angelman syndrome. Pediatr. Neurol. *48*, 271–279.

Tsakiridou, E., Bertollini, L., de Curtis, M., Avanzini, G., and Pape, H.C. (1995). Selective increase in T-type calcium conductance of reticular thalamic neurons in a rat model of absence epilepsy. J. Neurosci. *15*, 3110–3117.

van Woerden, G.M., Harris, K.D., Hojjati, M.R., Gustin, R.M., Qiu, S., de Avila Freire, R., Jiang, Y.H., Elgersma, Y., and Weeber, E.J. (2007). Rescue of neurological deficits in a mouse model for Angelman syndrome by reduction of alphaCaMKII inhibitory phosphorylation. Nat. Neurosci. *10*, 280–282.

Vazdarjanova, A., Ramirez-Amaya, V., Insel, N., Plummer, T.K., Rosi, S., Chowdhury, S., Mikhael, D., Worley, P.F., Guzowski, J.F., and Barnes, C.A. (2006). Spatial exploration induces ARC, a plasticity-related immediate-early gene, only in calcium/calmodulin-dependent protein kinase II-positive principal excitatory and inhibitory neurons of the rat forebrain. J. Comp. Neurol. *498*, 317–329.

Vendrame, M., Loddenkemper, T., Zarowski, M., Gregas, M., Shuhaiber, H., Sarco, D.P., Morales, A., Nespeca, M., Sharpe, C., Haas, K., et al. (2012). Analysis of EEG patterns and genotypes in patients with Angelman syndrome. Epilepsy Behav. *23*, 261–265.

Wallace, M.L., Burette, A.C., Weinberg, R.J., and Philpot, B.D. (2012). Maternal loss of Ube3a produces an excitatory/inhibitory imbalance through neuron type-specific synaptic defects. Neuron *74*, 793–800.

Weeber, E.J., Jiang, Y.H., Elgersma, Y., Varga, A.W., Carrasquillo, Y., Brown, S.E., Christian, J.M., Mirnikjoo, B., Silva, A., Beaudet, A.L., and Sweatt, J.D. (2003). Derangements of hippocampal calcium/calmodulin-dependent protein kinase II in a mouse model for Angelman mental retardation syndrome. J. Neurosci. *23*, 2634–2644.

Wei, W., Zhang, N., Peng, Z., Houser, C.R., and Mody, I. (2003). Perisynaptic localization of delta subunit-containing GABA(A) receptors and their activation by GABA spillover in the mouse dentate gyrus. J. Neurosci. *23*, 10650–10661.

Williams, C.A., Beaudet, A.L., Clayton-Smith, J., Knoll, J.H., Kyllerman, M., Laan, L.A., Magenis, R.E., Moncla, A., Schinzel, A.A., Summers, J.A., and Wagstaff, J. (2006). Angelman syndrome 2005: updated consensus for diagnostic criteria. Am. J. Med. Genet. A. *140*, 413–418.

Yamasaki, K., Joh, K., Ohta, T., Masuzaki, H., Ishimaru, T., Mukai, T., Niikawa, N., Ogawa, M., Wagstaff, J., and Kishino, T. (2003). Neurons but not glial cells show reciprocal imprinting of sense and antisense transcripts of Ube3a. Hum. Mol. Genet. *12*, 837–847.

Zhang, Y., Llinas, R.R., and Lisman, J.E. (2009). Inhibition of NMDARs in the Nucleus Reticularis of the Thalamus Produces Delta Frequency Bursting. Front. Neural Circuits *3*, 20.

Neuron, Volume *90*

Supplemental Information

GABAergic Neuron-Specific Loss of *Ube3a* Causes Angelman Syndrome-Like EEG Abnormalities and Enhances Seizure Susceptibility

Matthew C. Judson, Michael L. Wallace, Michael S. Sidorov, Alain C. Burette, Bin Gu, Geeske M. van Woerden, Ian F. King, Ji Eun Han, Mark J. Zylka, Ype Elgersma, Richard J. Weinberg, and Benjamin D. Philpot

Figure S1

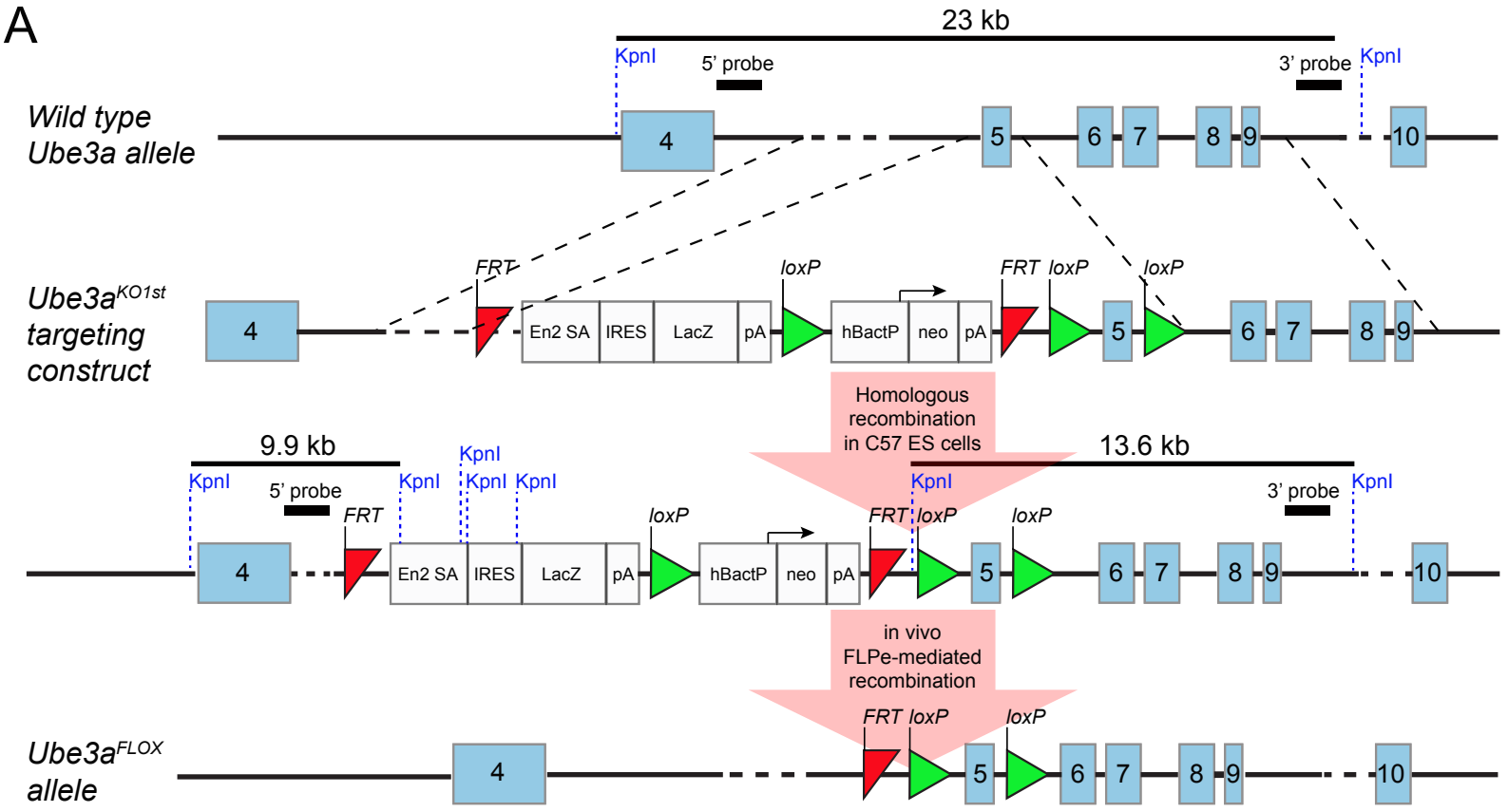

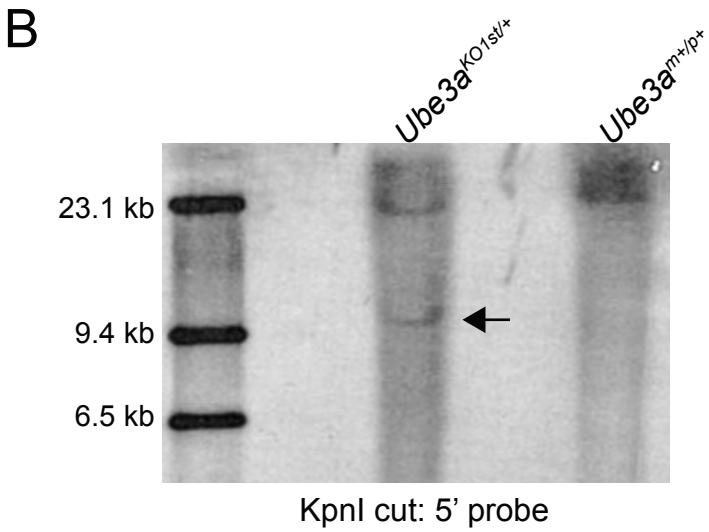

KpnI cut: 5' probe

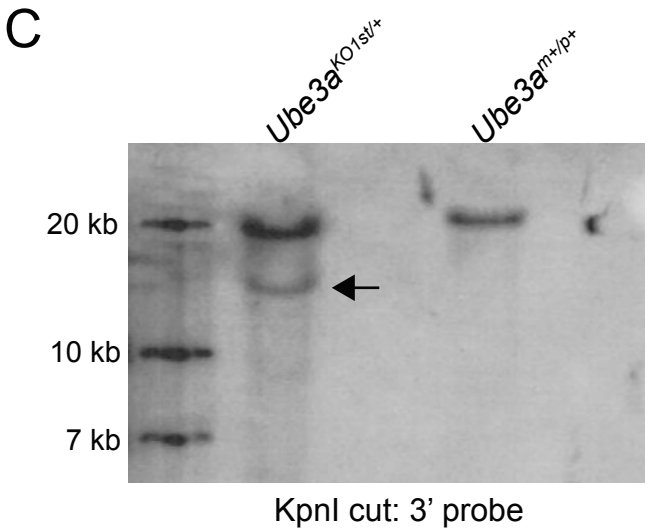

KpnI cut: 3' probe

Figure S2

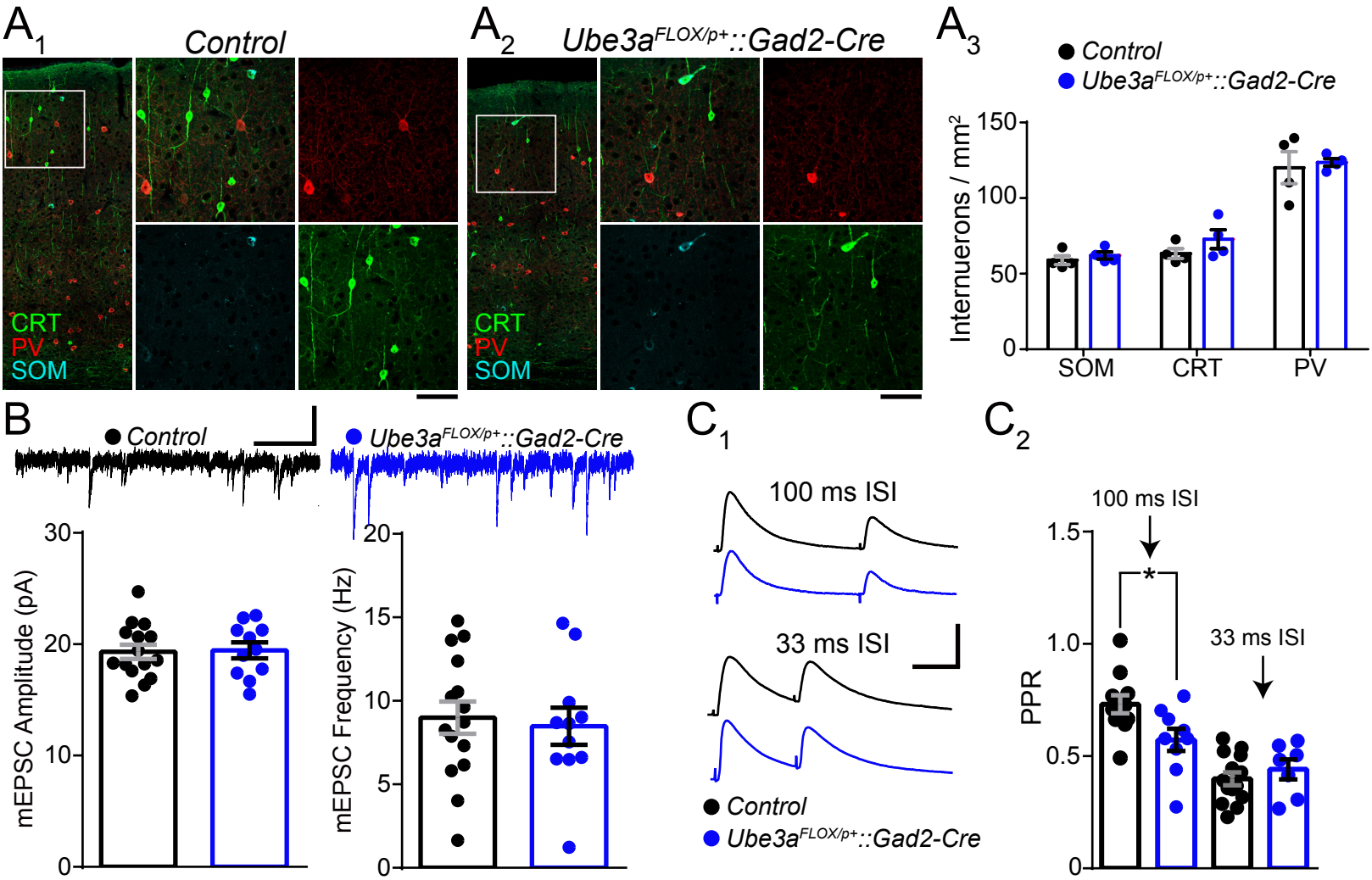
A1
Control
A2
Ube3aFLOX/p+::Gad2-Cre
A3
Control
Ube3aFLOX/p+::Gad2-Cre
CRT
PV
SOM
Interneurons / mm2
150
100
50
0
SOM
CRT
PV
B
Control
Ube3aFLOX/p+::Gad2-Cre
mEPSC Amplitude (pA)
30
20
10
0
mEPSC Frequency (Hz)
20
15
10
5
0
C1
100 ms ISI
33 ms ISI
Control
Ube3aFLOX/p+::Gad2-Cre
C2
100 ms ISI
33 ms ISI
PPR
1.5
1.0
0.5
0
*

Figure S3

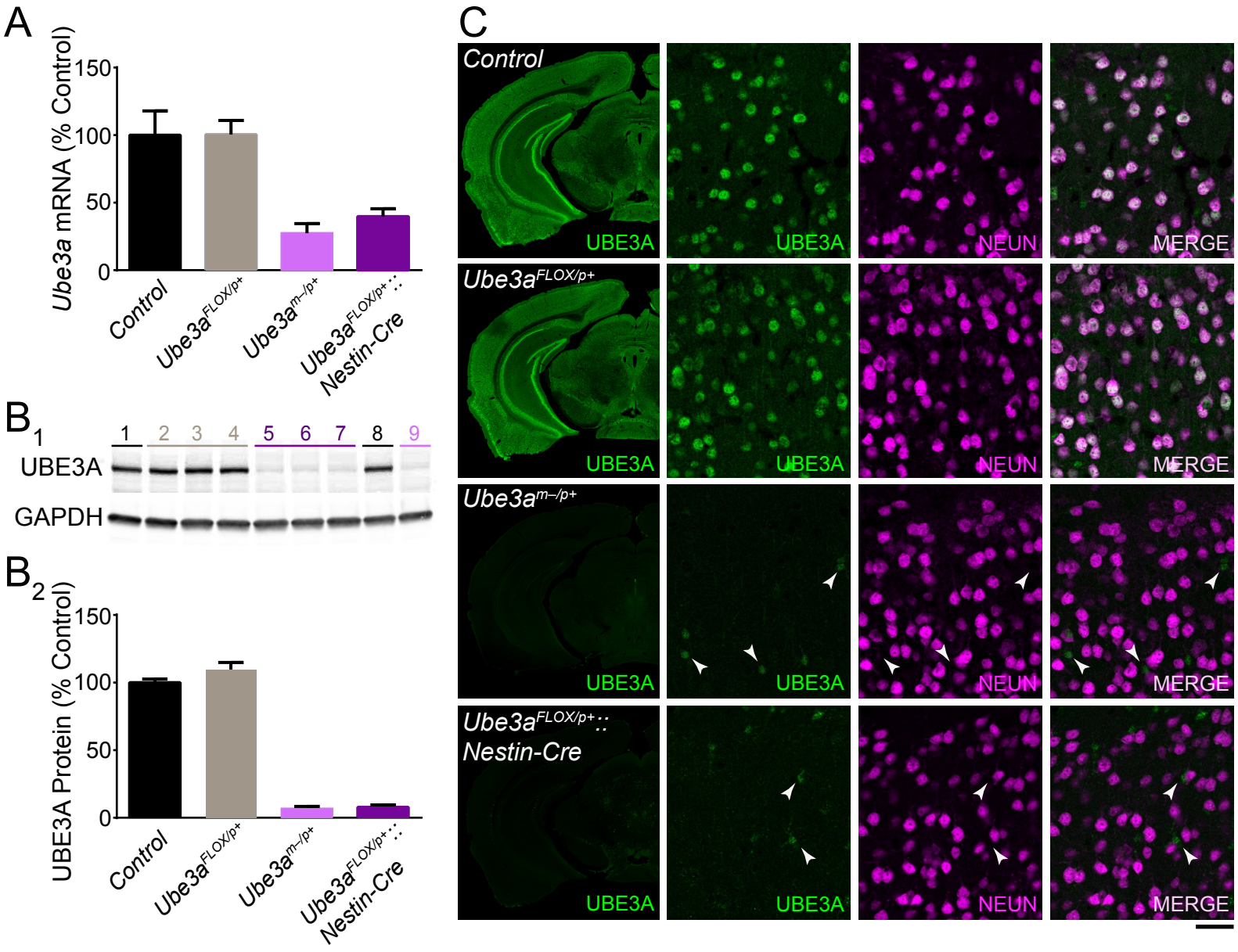
A
Ube3a mRNA (% Control)
150
100
50
0
Control
Ube3a FLOX/p+
Ube3a m−/p+
Ube3a FLOX/p+:: Nestin-Cre
B1
1 2 3 4 5 6 7 8 9
UBE3A
GAPDH
B2
UBE3A Protein (% Control)
150
100
50
0
Control
Ube3a FLOX/p+
Ube3a m−/p+
Ube3a FLOX/p+:: Nestin-Cre
C
Control
Ube3a FLOX/p+
Ube3a m−/p+
Ube3a FLOX/p+:: Nestin-Cre
UBE3A
NEUN
MERGE

Figure S4

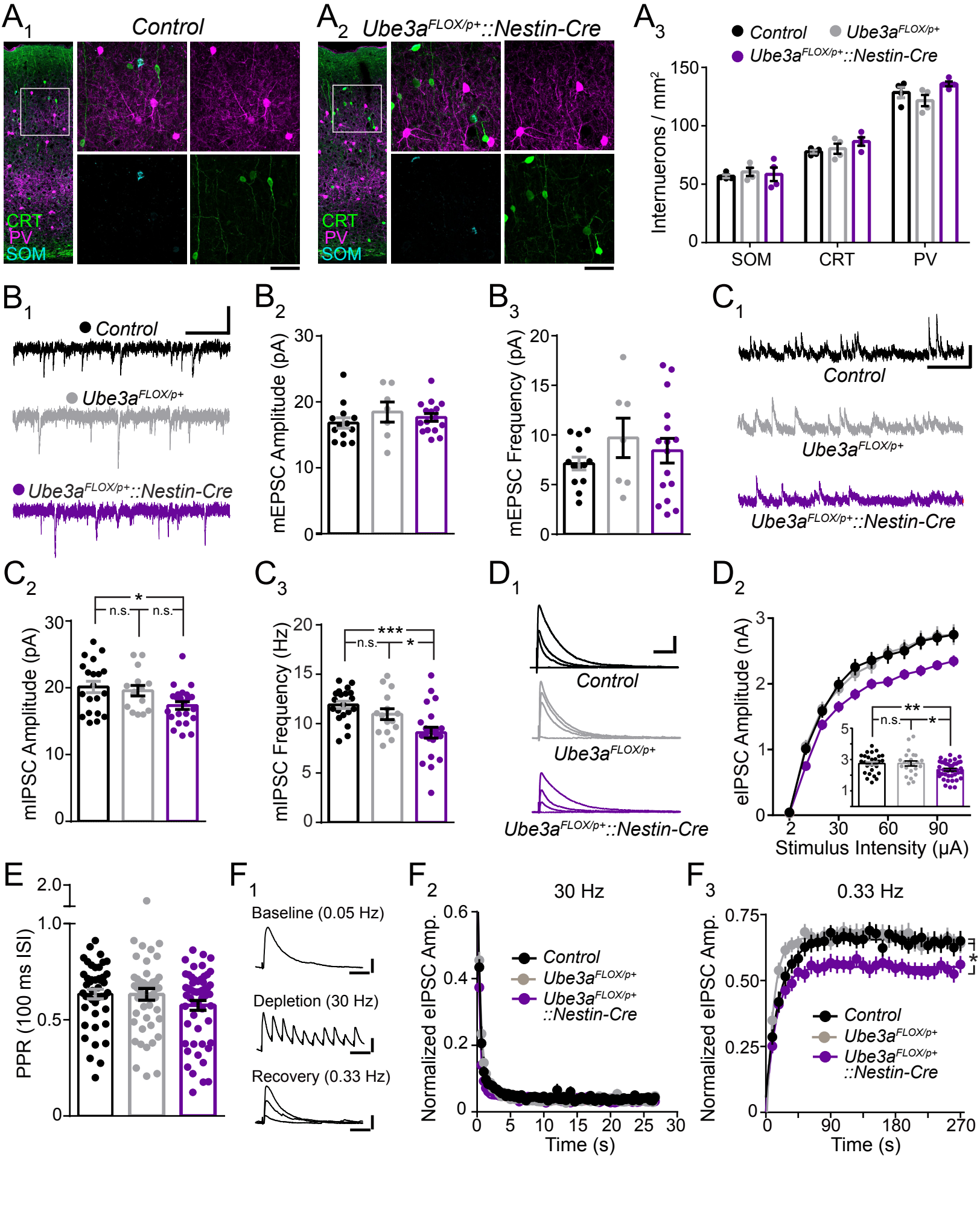
A1
Control
A2
Ube3aFLOX/p+::Nestin-Cre
CRT
PV
SOM
A3
Control
Ube3aFLOX/p+
Ube3aFLOX/p+::Nestin-Cre
Internuerons / mm2
150
100
50
0
SOM
CRT
PV
B1
Control
Ube3aFLOX/p+
Ube3aFLOX/p+::Nestin-Cre
B2
mEPSC Amplitude (pA)
30
20
10
0
B3
mEPSC Frequency (pA)
20
15
10
5
0
C1
Control
Ube3aFLOX/p+
Ube3aFLOX/p+::Nestin-Cre
C2
mIPSC Amplitude (pA)
*
n.s.
n.s.
30
20
10
0
C3
mIPSC Frequency (Hz)
***
n.s.
*
20
15
10
5
0
D1
Control
Ube3aFLOX/p+
Ube3aFLOX/p+::Nestin-Cre
D2
eIPSC Amplitude (nA)
3
2
1
0
**
n.s.
*
5
3
1
2
30
60
90
Stimulus Intensity (μA)
E
PPR (100 ms ISI)
2.0
1.0
0.5
0
F1
Baseline (0.05 Hz)
Depletion (30 Hz)
Recovery (0.33 Hz)
F2
30 Hz
Normalized eIPSC Amp.
0.6
0.4
0.2
0
Control
Ube3aFLOX/p+
Ube3aFLOX/p+
::Nestin-Cre
0
5
10
15
20
25
30
Time (s)
F3
0.33 Hz
Normalized eIPSC Amp.
0.75
0.50
0.25
0
*
Control
Ube3aFLOX/p+
Ube3aFLOX/p+
::Nestin-Cre
0
90
180
270
Time (s)

Figure S5

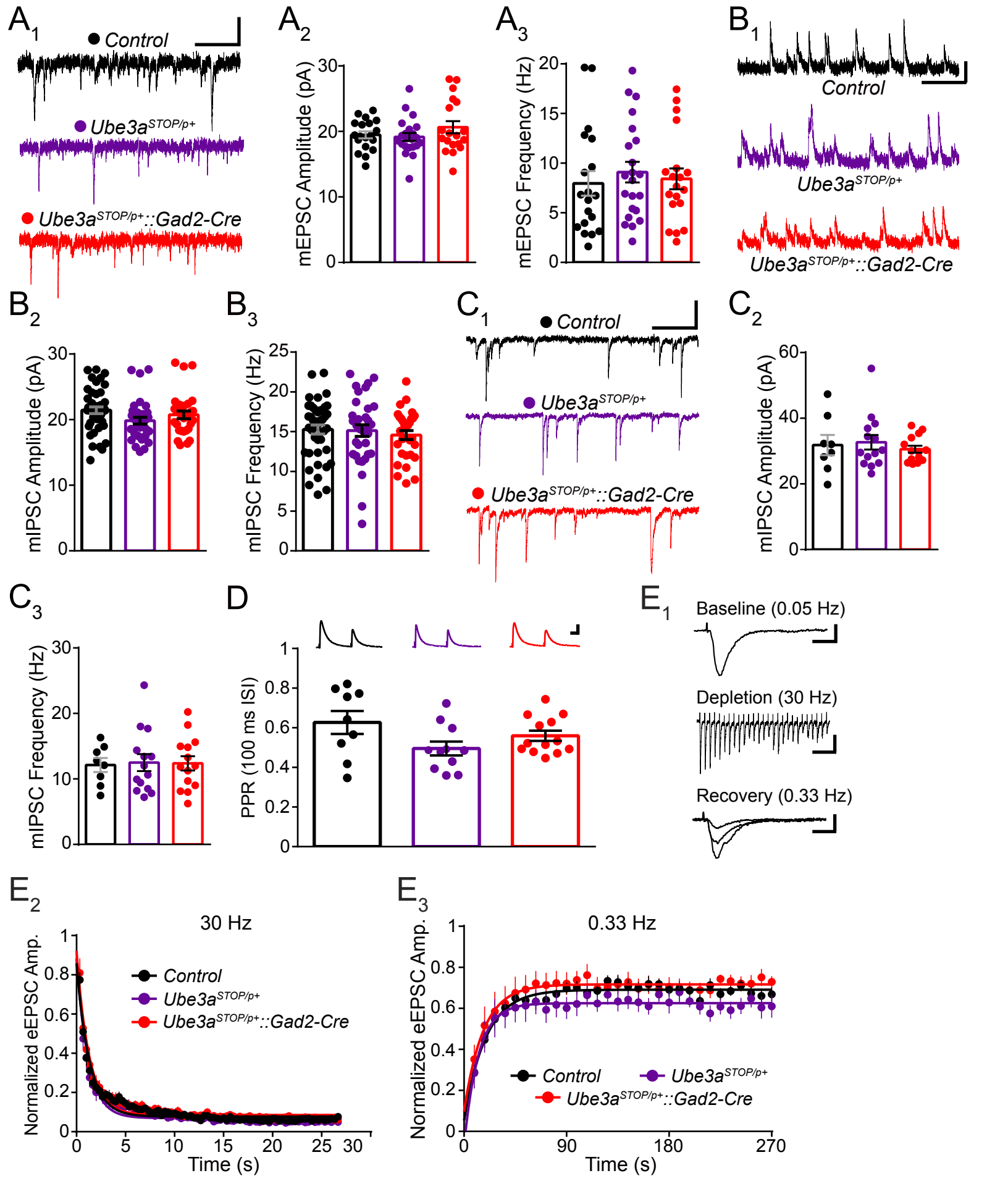
A1
Control
Ube3aSTOP/p+
Ube3aSTOP/p+::Gad2-Cre
A2
mEPSC Amplitude (pA)
A3
mEPSC Frequency (Hz)
B1
Control
Ube3aSTOP/p+
Ube3aSTOP/p+::Gad2-Cre
B2
mIPSC Amplitude (pA)
B3
mIPSC Frequency (Hz)
C1
Control
Ube3aSTOP/p+
Ube3aSTOP/p+::Gad2-Cre
C2
mIPSC Amplitude (pA)
C3
mIPSC Frequency (Hz)
D
PPR (100 ms ISI)
E1
Baseline (0.05 Hz)
Depletion (30 Hz)
Recovery (0.33 Hz)
E2
30 Hz
Normalized eEPSC Amp.
Control
Ube3aSTOP/p+
Ube3aSTOP/p+::Gad2-Cre
Time (s)
E3
0.33 Hz
Normalized eEPSC Amp.
Control
Ube3aSTOP/p+
Ube3aSTOP/p+::Gad2-Cre
Time (s)

Figure S6

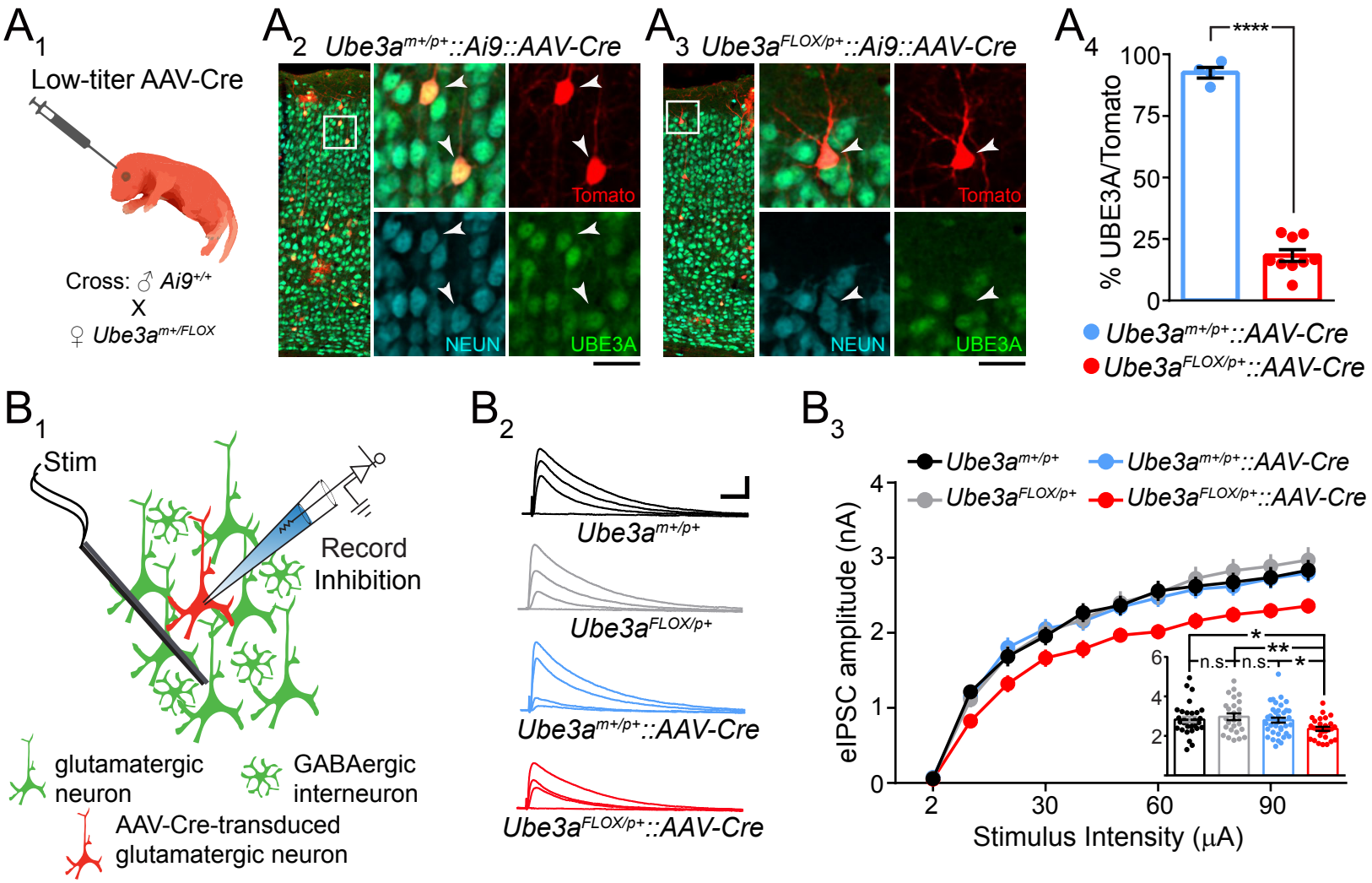
A1
Low-titer AAV-Cre
Cross: ♂ Ai9+/+
X
♀ Ube3am+/FLOX
A2 Ube3am+/p+::Ai9::AAV-Cre
Tomato
NEUN
UBE3A
A3 Ube3aFLOX/p+::Ai9::AAV-Cre
Tomato
NEUN
UBE3A
A4
****
% UBE3A/Tomato
100
75
50
25
0
Ube3am+/p+::AAV-Cre
Ube3aFLOX/p+::AAV-Cre
B1
Stim
Record
Inhibition
glutamatergic neuron
GABAergic interneuron
AAV-Cre-transduced glutamatergic neuron
B2
Ube3am+/p+
Ube3aFLOX/p+
Ube3am+/p+::AAV-Cre
Ube3aFLOX/p+::AAV-Cre
B3
Ube3am+/p+
Ube3aFLOX/p+
Ube3am+/p+::AAV-Cre
Ube3aFLOX/p+::AAV-Cre
eIPSC amplitude (nA)
Stimulus Intensity (μA)
n.s.
n.s.
*
**
*

Figure S7

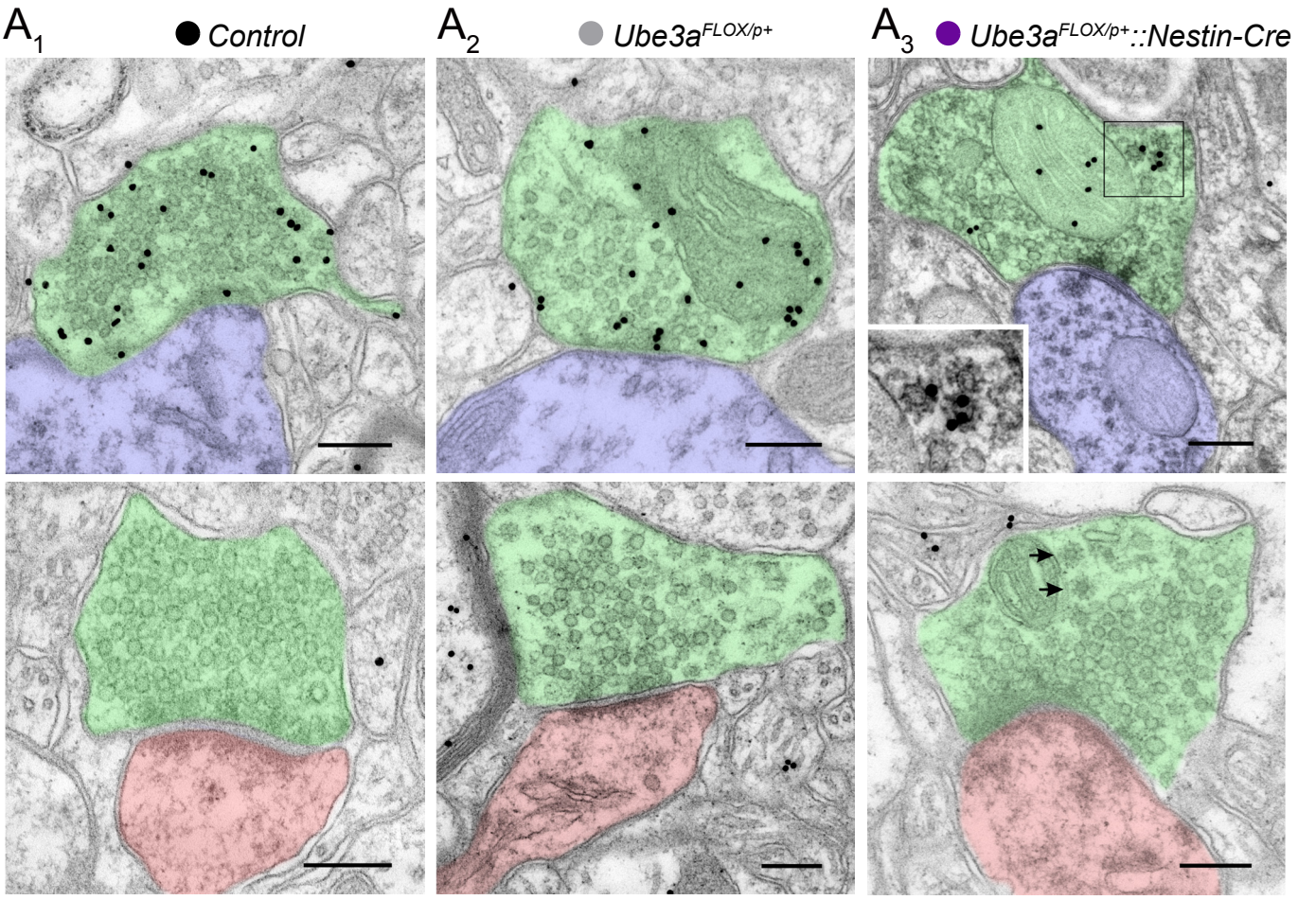
A1
Control
A2
Ube3aFLOX/p+
A3
Ube3aFLOX/p+::Nestin-Cre

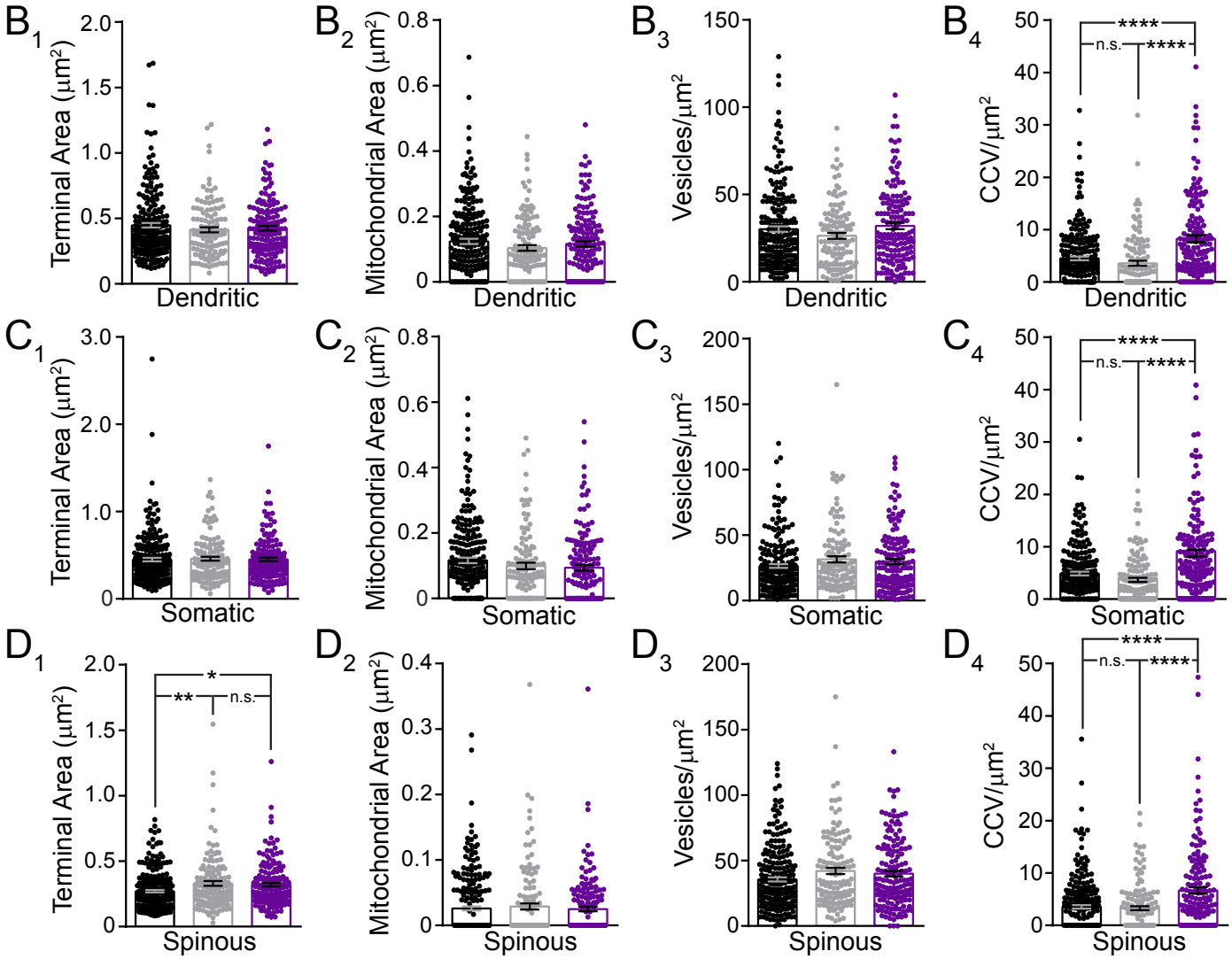
B1
Terminal Area (µm²)
Dendritic
B2
Mitochondrial Area (µm²)
Dendritic
B3
Vesicles/µm²
Dendritic
B4
CCV/µm²
****
n.s.
****
Dendritic
C1
Terminal Area (µm²)
Somatic
C2
Mitochondrial Area (µm²)
Somatic
C3
Vesicles/µm²
Somatic
C4
CCV/µm²
****
n.s.
****
Somatic
D1
Terminal Area (µm²)
*
**
n.s.
Spinous
D2
Mitochondrial Area (µm²)
Spinous
D3
Vesicles/µm²
Spinous
D4
CCV/µm²
****
n.s.
****
Spinous

Figure S8

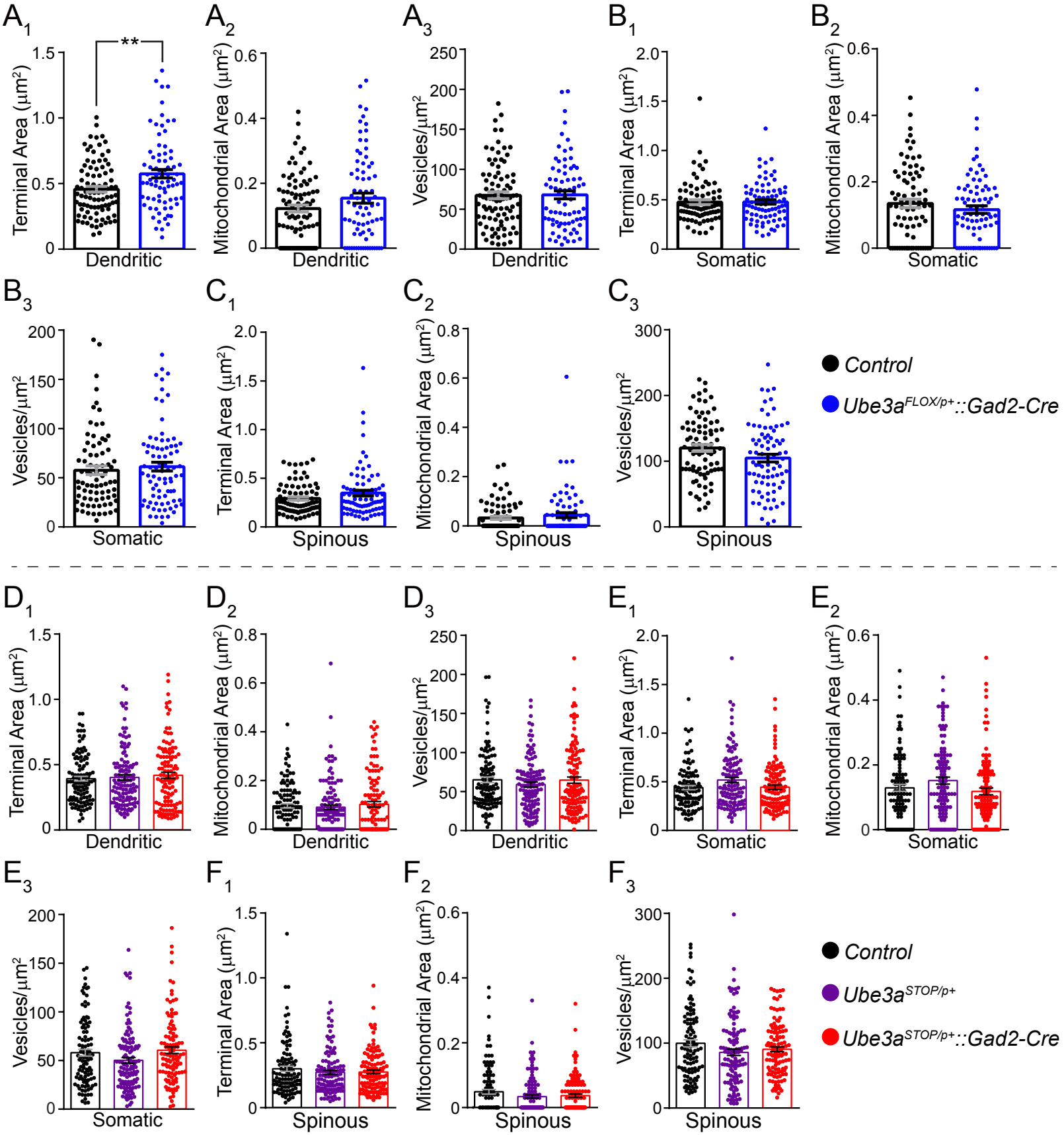
A1
A2
A3
B1
B2
B3
C1
C2
C3
D1
D2
D3
E1
E2
E3
F1
F2
F3
**
Terminal Area (µm²)
Mitochondrial Area (µm²)
Vesicles/µm²
Dendritic
Somatic
Spinous
Control
Ube3a^FLOX/p+::Gad2-Cre
Ube3a^STOP/p+
Ube3a^STOP/p+::Gad2-Cre

SUPPLEMENTAL FIGURE LEGENDS

Figure S1 (related to Figures 1, 3-7). Validation of *Ube3a^{KO1st}*-targeted embryonic stem cells.

(**A**) Schematic of strategy to generate C57BL/6 mice carrying the *Ube3a^{FLOX}* allele, as previously described (Berrios et al., 2016). (**B**) Southern blotting of genomic DNA from wild type (*Ube3a$^{m+/p+}$*) and *Ube3a^{KO1st}*-targeted embryonic stem cells. Probe specific to 5' end of the targeted *Ube3a* genomic region. (**C**) Southern blotting of the same samples using a probe specific to the 3' end of the targeted *Ube3a* genomic region. Arrows indicate KpnI-digested fragments specifically resulting from the *Ube3a^{KO1st}* allele.

Figure S2 (related to Figures 1 and 3). Analyses of interneuron density, miniature EPSCs, and evoked IPSC paired-pulse ratios following GABAergic deletion of *Ube3a*.

(**A**) Immunostaining of interneuron subtype-specific markers calretinin (CRT), parvalbumin (PV), and somatostatin (SOM) in ~P80 primary visual cortex of *Control* (A_1) and *Ube3a$^{FLOX/p+}$::Gad2-Cre* (A_2) mice. (A_3) Quantification of SOM-, CRT-, and PV-positive interneuron density (*Control* n = 4 mice; *Ube3a$^{FLOX/p+}$::Gad2-Cre* n = 4 mice). (**B**) Sample recordings and quantification of mEPSC amplitude and frequency from pyramidal neurons in ~P80 L2/3 visual cortex from *Control* (n = 15 cells) and *Ube3a$^{FLOX/p+}$::Gad2-Cre* (n = 11 cells) mice. (**C**) Sample recordings (C_1) and quantification (C_2) of eIPSC paired pulse ratios in ~P80 *Control* and *Ube3a$^{FLOX/p+}$::Gad2-Cre* mice using both 100 ms (*Control* n = 11 cells; *Ube3a$^{FLOX/p+}$::Gad2-Cre* n = 9 cells) and 33 ms (*Control* n = 14 cells; *Ube3a$^{FLOX/p+}$::Gad2-Cre* n = 7 cells) interstimulus intervals (ISI). Scale bars: 100 μm or 50 μm for zoom-ins (A); 20 pA, 200 ms (B); 200 pA, 20 ms (C_1, 100 ms ISI); 200 pA, 12 ms (C_1, 33 ms ISI). Data represent mean ± SEM. *p≤0.05.

Figure S3 (related to Figures 1, 3-7). Cre-mediated recombination of the maternally inherited *Ube3a^{FLOX}* allele nullifies neuronal *Ube3a* expression.

(**A**) qRT-PCR analysis of *Ube3a* expression in ~P60 neocortex (*Control* n = 6 mice; *Ube3a$^{FLOX/p+}$* n = 4 mice; *Ube3a$^{m-/p+}$* n = 3 mice; *Ube3a$^{FLOX/p+}$::Nestin-Cre* n = 4 mice). (**B**) Representative Western blots (B_1) for UBE3A and GAPDH loading control protein prepared from ~P60 neocortical lysates. Lanes: *Control* = 1 and 8; *Ube3a$^{FLOX/p+}$* = 2-4; *Ube3a$^{FLOX/p+}$::Nestin-Cre* = 5-7; *Ube3a$^{m-/p+}$* = 9. (B_2) Quantification of Western blotting (*Control* n = 3 mice; *Ube3a$^{FLOX/p+}$* n = 5 mice; *Ube3a$^{m-/p+}$* n = 2 mice; *Ube3a$^{FLOX/p+}$::Nestin-Cre* n = 6 mice). (**C**) UBE3A immunostaining at ~P80 in posterior coronal hemisections (far left column) and in L2/3 of primary visual cortex in conjunction with staining for the neuronal marker NEUN. Arrowheads indicate UBE3A staining in NEUN-negative glia (scale bar = 1.1 mm for hemisections and 35 μm for L2/3 visual cortex. Data represent mean ± SEM.

Figure S4 (related to Figures 1 and 3). Nervous system-specific deletion of maternal *Ube3a* results in inhibitory synaptic defects onto L2/3 pyramidal neurons.

(**A**) Immunostaining of interneuron subtype-specific markers calretinin (CRT), parvalbumin (PV), and somatostatin (SOM) in ~P80 primary visual cortex of *Control* (A_1) and *Ube3a$^{FLOX/p+}$::Nestin-Cre* (A_2) mice. Scale bar = 100 μm or 40 μm for zoom-ins. (A_3) Quantification of SOM-, CRT-, and PV-positive interneuron density (*Control* n = 4 mice; *Ube3a$^{FLOX/p+}$* n = 4 mice; *Ube3a$^{FLOX/p+}$::Nestin-Cre* n = 4 mice). (**B**) Sample recordings (B_1, scale bar = 20 pA, 200 ms) and quantification of mEPSC amplitude (B_2) and frequency (B_3) from pyramidal neurons in ~P80 L2/3 visual cortex from *Control* (n = 13 cells), *Ube3a$^{FLOX/p+}$* (n = 7 cells), and *Ube3a$^{FLOX/p+}$::Nestin-Cre* (n = 16 cells). (**C**) Sample mIPSC recordings (C_1) from pyramidal neurons in ~P80 L2/3 visual cortex (scale bar = 20 pA, 200 ms). Quantification of mIPSC amplitude (C_2) and frequency (C_3) (*Control* n = 20 cells; *Ube3a$^{FLOX/p+}$* n = 15 cells; *Ube3a$^{FLOX/p+}$::Nestin-Cre* n = 23 cells). (**D**) Sample recordings of eIPSCs (D_1) at stimulation intensities of 2, 10, 30, and 100 μA (scale bar = 900 pA, 50 ms). (D_2) Quantification of

eIPSCs at ~P80. Inset depicts response amplitudes to 100 μA stimulation (*Control* n = 28 cells; *Ube3a*$^{FLOX/p+}$ n = 23 cells; *Ube3a*$^{FLOX/p+}$*::Nestin-Cre* n = 40 cells). (**E**) Quantification of eIPSCs in paired-pulse experiments (*Control* n = 44 cells; *Ube3a*$^{FLOX/p+}$ n = 51 cells; *Ube3a*$^{FLOX/p+}$*::Nestin-Cre* n = 54 cells). (**F**) Sample recordings (F_1) depicting each phase of an inhibitory synaptic depletion and recovery experiment performed in ~P80 mice (scale bars: baseline = 200 pA, 20 ms; depletion = 200 pA, 70 ms; recovery = 200 pA, 20 ms). (F_2) Average depletion phase showing eIPSC amplitude normalized to baseline during 800 stimuli at 30 Hz. Each point (80 plotted per genotype) represents the average of 10 consecutive responses that were collapsed and averaged per cell. (F_3) Average recovery phase showing eIPSC amplitude normalized to baseline during 90 stimuli at 0.33 Hz. Each point (30 plotted per genotype) represents the average of 3 consecutive responses that were collapsed and averaged per cell. Average depletion and recovery responses for each genotype were fit with a monophasic exponential (*Control* n = 43 cells; *Ube3a*$^{FLOX/p+}$ n = 51 cells; *Ube3a*$^{FLOX/p+}$*::Nestin-Cre* n = 53 cells). Data represent mean ± SEM. *p≤0.05, ***p≤0.001.

Figure S5 (related to Figure 2). Analyses of miniature EPSCs, miniature IPSCs, evoked IPSC paired-pulse ratios, and excitatory synaptic depletion following GABAergic reinstatement of *Ube3a*.

(**A**) Sample recordings (A_1, scale bar = 20 pA, 200 ms) and quantification of mEPSC amplitude (A_2) and frequency (A_3) from pyramidal neurons in ~P80 L2/3 visual cortex from *Control* (n = 19 cells), *Ube3a*$^{STOP/p+}$ (n = 22 cells), and *Ube3a*$^{STOP/p+}$*::Gad2-Cre* (n = 19 cells). (**B**) Sample mIPSC recordings, using a standard internal solution (B_1), from pyramidal neurons in ~P80 L2/3 visual cortex (scale bar = 20 pA, 200 ms), with quantification of mIPSC amplitude (B_2) and frequency (B_3) (*Control* n = 43 cells; *Ube3a*$^{STOP/p+}$ n = 34 cells; *Ube3a*$^{STOP/p+}$*::Gad2-Cre* n = 30 cells). (**C**) Sample mIPSC recordings, using a high-chloride internal solution (C_1), from pyramidal neurons in ~P80 L2/3 visual cortex (scale bar = 50 pA, 200 ms), with quantification of mIPSC amplitude (C_2) and mIPSC

frequency (C_3) (*Control* n = 8 cells; *Ube3a*$^{STOP/p+}$ n = 14 cells; *Ube3a*$^{STOP/p+}$*::Gad2-Cre* n = 14 cells). (**D**) Sample recordings (scale bar = 200 pA, 25 ms) and quantification of eIPSCs in paired-pulse experiments (*Control* n = 9 cells; *Ube3*$^{STOP/p+}$ n = 11 cells; *Ube3a*$^{STOP/p+}$*::Gad2-Cre* n = 13 cells). (**E**) Sample recordings (E_1) depicting each phase of an excitatory synaptic depletion and recovery experiment performed in ~P80 mice (scale bars: baseline = 60 pA, 8 ms; depletion = 60 pA, 160 ms; recovery = 60 pA, 8 ms). (E_2) Average depletion phase showing eEPSC amplitude normalized to baseline during 800 stimuli at 30 Hz. Each point (80 plotted per genotype) represents the average of 10 consecutive responses that were collapsed and averaged per cell. (E_3) Average recovery phase showing eEPSC amplitude normalized to baseline during 90 stimuli at 0.33 Hz. Each point (30 plotted per genotype) represents the average of 3 consecutive responses that were collapsed and averaged per cell. Average depletion and recovery responses for each genotype were fit with a monophasic exponential (*Control* n = 13 cells; *Ube3a*$^{STOP/p+}$ n = 11 cells; *Ube3a*$^{STOP/p+}$*::Gad2-Cre* n = 11 cells). Data represent mean ± SEM.

Figure S6 (related to Figure 3). Decreased evoked IPSC amplitude following cell-autonomous glutamatergic *Ube3a* loss.

(**A**) Intracerebroventricular injection strategy (A_1) used to achieve mosaic AAV-Cre transduction of L2/3 pyramidal neurons in *Ube3a*$^{FLOX/p+}$ and *Ube3a*$^{m+/p+}$ control littermates expressing the *Ai9* Cre-dependent tdTomato reporter allele. Immunostaining of UBE3A and the neuronal marker NEUN in P12 *Ube3a*$^{m+/p+}$*::Ai9* (A_2) and *Ube3a*$^{FLOX/p+}$*::Ai9* (A_3) mice neonatally injected with low-titer AAV-Cre. Arrowheads point to AAV-Cre-transduced, tdTomato-positive L2/3 pyramidal neurons (scale bar = 125 μm or 30 μm for zoom-ins). (A_4) Quantification at P12 of the percentage of tdTomato and UBE3A co-stained neurons per 800 μm-wide strip of cortex (*Ube3a*$^{m+/p+}$ n = 5 strips; *Ube3a*$^{FLOX/p+}$ n = 10 strips). (**B**) Schematic for recording eIPSCs (B_1) from L2/3 pyramidal neurons in AAV-Cre-transduced primary visual cortex. (B_2) Sample recordings of eIPSCs at stimulation intensities of 2, 10, 30, and

100 μA (scale bar = 1 nA, 40 ms). (B_3) Quantification of eIPSCs recorded at ~P80. Inset depicts response amplitudes to 100 μA stimulation (*Ube3a*$^{m+/p+}$ n = 32 cells; *Ube3a*$^{FLOX/p+}$ n = 26 cells; *Ube3a*$^{m+/p+}$*::AAV-Cre* n = 38 cells; *Ube3a*$^{FLOX/p+}$*::AAV-Cre* n = 28 cells). Data represent mean ± SEM. *p≤0.05, **p≤0.01, ****p≤0.0001.

Figure S7 (related to Figure 7). Nervous system-specific deletion of *Ube3a* causes CCV accumulation at both glutamatergic and GABAergic neocortical synapses.

(**A**) Electron micrographs of dendritic inhibitory synapses stained for GABA (top row) and glutamatergic spinous synapses (bottom row) in *Control* (A_1), *Ube3a*$^{FLOX/p+}$ (A_2), and *Ube3a*$^{FLOX/p+}$*::Nestin-Cre* (A_3) mice at ~P80. Green denotes GABAergic axon terminal, blue denotes dendrite, red denotes dendritic spine, inset or arrows highlight clathrin coated vesicles (CCVs) (scale bar = 200 nm). (**B**) Average values at dendritic inhibitory synapses for axon terminal area (B_1), terminal mitochondrial area (B_2), synaptic vesicles per μm^2 (B_3), and CCVs per μm^2 (B_4) (*Control* n = 216 synapses from 6 mice; *Ube3a*$^{FLOX/p+}$ n = 117 synapses from 3 mice; *Ube3a*$^{FLOX/p+}$*::Nestin-Cre* n = 151 synapses from 4 mice). (**C**) Average values at somatic inhibitory synapses for axon terminal area (C_1), terminal mitochondrial area (C_2), synaptic vesicles per μm^2 (C_3), and CCVs per μm^2 (C_4) (*Control* n = 213 synapses from 6 mice; *Ube3a*$^{FLOX/p+}$ n = 123 synapses from 3 mice; *Ube3a*$^{FLOX/p+}$*::Nestin-Cre* n = 149 synapses from 4 mice). (**D**) Average values at glutamatergic (spinous) synapses for axon terminal area (D_1), terminal mitochondrial area (D_2), synaptic vesicles per μm^2 (D_3), and CCVs per μm^2 (D_4) (*Control* n = 241 synapses from 6 mice; *Ube3a*$^{FLOX/p+}$ n = 132 synapses from 3 mice; *Ube3a*$^{FLOX/p+}$*::Nestin-Cre* n = 156 synapses from 4 mice). Data represent mean ± SEM. *p≤0.05, **p≤0.01, ****p≤0.0001.

Figure S8 (related to Figure 7). Ultrastructural analyses of presynaptic terminal size, mitochondrial representation, and synaptic vesicle density following GABAergic *Ube3a* deletion and reinstatement.

(**A-C**) Average values from ~P80 *Control* and *Ube3a*$^{FLOX/p+}$*::Gad2-Cre* mice at L2/3 GABAergic synapses onto dendrites (A_1-A_3, *Control* n = 89 synapses from 3 mice; *Ube3a*$^{FLOX/p+}$*::Gad2-Cre* n = 77 synapses from 3 mice), L2/3 GABAergic synapses onto somata (B_1-B_3, *Control* n = 78 synapses from 3 mice; *Ube3a*$^{FLOX/p+}$*::Gad2-Cre* n = 81 synapses from 3 mice), and L2/3 glutamatergic spinous synapses (C_1-C_3, *Control* n = 82 synapses from 3 mice; *Ube3a*$^{FLOX/p+}$*::Gad2-Cre* n = 80 synapses from 3 mice). (**D-F)** Average values from ~P80 *Control*, *Ube3a*$^{STOP/p+}$, and *Ube3a*$^{STOP/p+}$*::Gad2-Cre* mice at L2/3 GABAergic synapses onto dendrites (D_1-D_3, *Control* n = 110 synapses from 3 mice; *Ube3a*$^{STOP/p+}$ n = 119 synapses from 3 mice; *Ube3a*$^{STOP/p+}$*::Gad2-Cre* n = 115 synapses from 3 mice), L2/3 GABAergic synapses onto somata (E_1-E_3, *Control* n = 103 synapses from 3 mice; *Ube3a*$^{STOP/p+}$ n = 114 synapses from 3 mice; *Ube3a*$^{STOP/p+}$*::Gad2-Cre* n = 110 synapses from 3 mice), and L2/3 glutamatergic spinous synapses (F_1-F_3, *Control* n = 108 synapses from 3 mice; *Ube3a*$^{STOP/p+}$ n = 113 synapses from 3 mice; *Ube3a*$^{STOP/p+}$*::Gad2-Cre* n = 113 synapses from 3 mice). Data represent mean ± SEM. **p≤0.01.

Table S1 (related to Figures 1, 3, S4, and S5). Quantification of membrane properties from mIPSC experiments

Figure S4C (mIPSCs)				
Genotype:	*Control*	*Ube3a$^{FLOX/p+}$*	*Ube3a$^{FLOX/p+}$::Nestin-Cre*	p-value
n =	20	15	23	
*Cm (pF)	169.9 ± 7.5	158.86 ± 8.65	156.35 ± 5.47	0.34
Rs (MΩ)	14.7 ± 0.84	14.62 ± 0.6	13.99 ± 0.69	0.74
Rm (MΩ)	213.2 ± 15.8	236.26 ± 16.1	241.26 ± 16.12	0.41
*Tau (ms)	1.9 ± 0.13	1.8 ± 0.14	1.8 ± 0.1	0.86
Figure 1C (mIPSCs)				
Genotype:	*Control*	*Ube3a$^{FLOX/p+}$::Gad2-Cre*	p-value	
n =	11	17		
*Cm (pF)	167.45 ± 8.83	162.53 ± 6.79	0.66	
Rs (MΩ)	13.98 ± 1.31	13.72 ± 0.86	0.87	
Rm (MΩ)	218.92 ± 26.12	223.87 ± 5.91	0.82	
*Tau (ms)	1.59 ± 0.17	1.62 ± 0.1	0.64	
Figure 3F (mIPSCs)				
Genotype:	*Control*	*Ube3a$^{FLOX/p+}$::NEX-Cre*	p-value	
n =	15	12		
*Cm (pF)	152.07 ± 5.66	157.75 ± 9.73	0.62	
Rs (MΩ)	15.52 ± 1.12	16.08 ± 1.49	0.77	
Rm (MΩ)	188.13 ± 8.57	195.5 ± 14.83	0.67	
*Tau (ms)	2.17 ± 0.16	2.2 ± 0.19	0.90	
Figure S5B (mIPSCs)				
Genotype:	*Control*	*Ube3a$^{STOP/p+}$*	*Ube3a$^{STOP/p+}$::Gad2-Cre*	p-value
n =	43	34	30	
*Cm (pF)	174.11 ± 4.39	165.9 ± 4.95	173.96 ± 7.0	0.47
Rs (MΩ)	11.13 ± 0.54	11.09 ± 0.61	10.91 ± 0.64	0.97
Rm (MΩ)	183.13 ± 8.06	186.45 ± 9.82	189.51 ± 10.15	0.89
*Tau (ms)	1.78 ± 0.08	1.71 ± 0.1	1.74 ± 0.08	0.83

Cm, capacitance; Rs, series resistance; Rm, membrane resistance; Tau, membrane time constant. *Values estimated using membrane test feature in pClamp 10.

SUPPLEMENTAL EXPERIMENTAL PROCEDURES

Animals

We generated *Ube3a*^{FLOX} mice in the UNC Animal Models Core facility. Briefly, we electroporated C57BL/6 mouse embryonic stem (ES) cells with an AsiSI-linearized *Ube3a*^{KO1st} targeting construct, which was generated by the trans-NIH Knockout Mouse Project (KOMP) and obtained from the KOMP repository (www.komp.org). We then analyzed DNA from neomycin-resistant ES cell colonies by Southern blot hybridization using both 5'- and 3'-flanking probes to confirm clones which had incorporated the *Ube3a*^{KO1st} allele via homologous recombination. To produce *Ube3a*^{KO1st}-targeted chimeric mice, we microinjected *Ube3a*^{KO1st}-targeted ES cells into C57BL/6-albino blastocysts. We then crossed germline chimeric males (determined by transmission of coat color in parallel breeding) to C57BL/6 female homozygous *Rosa26-FLPe* mice (RRID:IMSR_JAX:009086) in order to excise the *FRT*-flanked lacZ gene trap from the *Ube3a*^{KO1st} allele and thereby produce the conditional *Ube3a* knockout allele (i.e., *Ube3a*^{FLOX}). We bred the *FLPe* allele out of the *Ube3a*^{FLOX} line and maintained *Ube3a*$^{m+/FLOX}$ female breeders on a congenic C57BL/6 background, except for *in vivo* LFP and audiogenic seizure experiments, in which case *Ube3a*$^{m+/FLOX}$ female breeders were backcrossed at least 5 times onto the129S2/SvPasCrl background. We genotyped *Ube3a*^{FLOX} mice using the following polymerase chain reaction (PCR) primers: *Ube3a*^{FLOX} F (5′- AAAATTGGGTATGCGAGCTG -3′) and *Ube3a*^{FLOX} R (5′- GGGGTCTAAGGGCCTATGAA -3′).

The laboratory of Ype Elgersma originally generated *Ube3a*^{STOP} mice on a congenic 129S2/SvPasCrl background (Silva-Santos et al., 2015). We maintained *Ube3a*$^{m+/STOP}$ females on the congenic 129S2/SvPasCrl background to support breeding for *in vivo* LFP recordings and audiogenic seizure experiments, but used *Ube3a*$^{m+/STOP}$ females backcrossed 2-4 generations onto the C57BL/6J background for breeding to supply whole-cell electrophysiology and electron microscopy experiments.

Most experiments required the mating of female mice with paternal inheritance of a conditional *Ube3a* allele (i.e., *Ube3a*$^{m+/FLOX}$ or *Ube3a*$^{m+/STOP}$) to heterozygous males from one of three *Cre*-expressing lines: *Nestin-Cre* mice (RRID:IMSR_JAX:003771) (Tronche et al., 1999), *Gad2-Cre* mice (RRID:IMSR_JAX:010802), or *NEX-Cre* mice (Goebbels et al., 2006), which Klaus-Armin Nave generously provided.

We maintained *Nestin-Cre* and *NEX-Cre* mice on a congenic C57BL/6 background. We always bred *Nestin-Cre* males to congenic C57BL/6 *Ube3a*$^{m+/FLOX}$ females to yield congenic C57BL/6 experimental offspring. The same was true for *NEX-Cre* breeding with regard to generation of congenic C57BL/6 animals for histology, electrophysiology experiments, and *Ube3a*$^{FLOX/p+}$*::NEX-Cre* offspring for flurothyl seizure assays.

Gad2-Cre mice were initially generated as C57/129 hybrids (Taniguchi et al., 2011), which had been backcrossed at least 3 generations toward C57BL/6 prior to our acquiring them from JAX. We used *Gad2-Cre* males backcrossed at least 4 times onto C57BL/6 to breed mice for whole-cell electrophysiology and electron microscopy experiments, and at least 7 times onto C57BL/6 to breed for flurothyl seizure assays. For *in vivo* LFP recordings and audiogenic seizure experiments, we used *Gad2-Cre* breeder males backcrossed at least 5 generations back toward 129S2/SvPasCrl when bred to congenic 129S2/SvPasCrl *Ube3a*$^{m+/STOP}$ females and *Gad2-Cre* breeder males backcrossed at least 9 generations back toward 129S2/SvPasCrl when crossed to 5x 129-backcrossed *Ube3a*$^{m+/FLOX}$ females (see above).

To generate litters for AAV-Cre injections, we crossed *Ube3a*$^{m+/FLOX}$ females to male homozygous *Ai9*, tdTomato Cre-reporter mice (RRID:IMSR_JAX:007909), which were maintained on a congenic C57BL/6 background (Madisen et al., 2010). We generated constitutively maternal *Ube3a*-deficient mice (*Ube3a*$^{m-/p+}$) by breeding congenic C57BL/6 *Ube3a*$^{m+/p-}$ females (RRID:IMSR_JAX:016590) to congenic C57BL/6 wild type males (Jiang et al., 1998).

Adeno-Associated Virus (AAV) Injections

We cryoanesthetized P0-P1.5 mouse pups on wet ice for ~3 minutes before transferring them to a chilled stage equipped with a fiber optic light source to transilluminate the lateral ventricles. We used a 10 μl syringe with a 32-gauge, 0.4 inch-long sterile syringe needle (7803-04, Hamilton, Reno, NV) to bilaterally deliver 0.5 μL of purified AAV (4 x 10^{12} viral genomes/mL) to the lateral ventricles. We added fast green dye (1 mg/mL) to the virus solution to verify successful injections. This procedure resulted in ~4 x 10^{9} total viral genomes being injected per pup. We specifically used AAV vectors with the serotype 9 capsid, which were packaged at the UNC Viral Vector Core with self-complementary genomes containing a modified hybrid CMV enhancer/chicken b-actin (CBh) promoter driving a Cre expression cassette (Gray et al., 2011). Following injection, we warmed pups on an isothermal heating pad with home-cage nesting material before returning them *en masse* to their typical home cage environment.

Electrophysiology

Acute coronal slice preparation. We anesthetized P70-P90 mice with pentobarbital (40 mg/kg) and, after confirming the disappearance of corneal reflexes, transcardially perfused them with ice-cold dissection buffer (in mM: 87 NaCl, 2.5 KCl, 1.25 $NaH2PO_4$, 26 $NaHCO_3$, 75 sucrose, 10 dextrose, 1.3 ascorbic acid, 7 $MgCl_2$, and 0.5 $CaCl_2$) bubbled with 95% O_2 and 5% CO_2. We then dissected the visual cortices and prepared 350 μm-thick coronal slices using a VT1000S vibrating microtome (Leica, Buffalo Grove, IL). We allowed slices to recover for 20 minutes in a 35º C submersion chamber filled with oxygenated artificial cerebrospinal fluid (ACSF) (in mM; 124 NaCl, 3 KCl, 1.25 $NaH2PO_4$, 26 $NaHCO_3$, 1 $MgCl_2$, 2 $CaCl_2$, and 20 dextrose), which we supplemented with 1.25 mM ascorbic acid. We then transferred the recovery chamber to room temperature where slices remained for a minimum of 40 minutes prior to use (Philpot et al., 2003).

Miniature excitatory and inhibitory postsynaptic current (mEPSC and mIPSC) recording conditions. In order to pharmacologically block action potential firing, inhibitory neurotransmission, and to isolate AMPA (α-Amino-3-hydroxy-5-methyl-4-isoxazolepropionic acid) receptor-mediated mEPSCs, we perfused slices with 30º C, oxygenated ACSF containing 1 μM tetrodotoxin (TTX), 50 μM picrotoxin, and 100 μM D,L-2-amino-5-phosphonopentanoic acid (APV), and we performed recordings holding at -70 mV. For mIPSC experiments, we utilized ACSF containing 1 μM TTX, 20 μM 6,7-dinitroquinoxaline-2,3-dione (DNQX), and 100 μM APV. For most mIPSC experiments, we voltage-clamped neurons at 0 mV to maximize the chloride driving force for our standard Cs-based internal solutions. However, in a subset of experiments, we also used the following high chloride internal solution to more easily resolve mIPSCs (in mM): 2 NaCl, 141 KCl, 1 $CaCl_2$, 10 EGTA, 2 Mg-ATP, 0.3 Na-GTP, 10 HEPES, 10 Na-phosphocreatine, and 0.025 Alexa-594 with pH adjusted to 7.25 and osmolarity adjusted to ~295 mOsm with sucrose. We held neurons at -80 mV when using this internal.

Evoked inhibitory postsynaptic current (eIPSC) recording conditions. We recorded eIPSCs under identical conditions to those described for mIPSC experiments utilizing the Cs-based internal solution and a 0 mV holding potential, except that we withheld TTX from the ACSF to enable action potential firing. We electrically evoked IPSCs using a concentric bipolar stimulating electrode (200 μm tip separation) placed ~150 μm ventral to the recorded pyramidal neuron in L2/3. The duration of each electrical stimulus was 200 μs.

Evoked excitatory postsynaptic current (eEPSC) recording conditions. We recorded eEPSCs under identical conditions to those described for mEPSC experiments with two notable exceptions: 1) we excluded TTX and picrotoxin from the ACSF, and 2) we voltage clamped neurons at ~-45 mV (the empirically determined chloride reversal potential without adjusting for junction potential). Following the completion of excitatory synaptic depletion and recovery experiments we washed on DNQX and APV to confirm we were holding at the reversal potential for chloride; we excluded neurons from

analysis if their eEPSC amplitude did not decrease to at least 20% of the recovery plateau. We performed electrical stimulation as described for eIPSC recordings.

Tonic inhibitory current recording conditions. We recorded δ-$GABA_AR$-mediated tonic currents in ACSF containing 20 μM DNQX and 100 μM APV while voltage clamping at -70 mV using a CsCl internal solution (in mM: 135 CsCl, 2.5 $MgCl_2$, 10 HEPES, 4 NaATP, 0.4 NaGTP, 10 NaCreatine, 0.6 EGTA, and 0.025 Alexa-594 with pH adjusted to 7.25 and osmolarity adjusted to ~295 mOsm with sucrose). We activated δ-$GABA_AR$-selective currents via bath application of 1 μM 4,5,6,7-Tetrahydroisoxazolo[5,4-*c*]pyridin-3-ol hydrochloride (THIP/Gaboxadol) for 10 minutes, chased for 10 minutes with 20 μM 6-Imino-3-(4-methoxyphenyl)-1(6*H*)-pyridazinebutanoic acid hydrobromide (SR95531/Gabazine), a pan-$GABA_AR$ competitive antagonist. We quantified δ-$GABA_AR$-mediated currents both by measuring the inward shift in the holding current ($I_{holding}$) following wash-on of THIP (mean $I_{holding}$ from last 2 minutes of THIP wash-on – mean $I_{holding}$ from last 2 minutes of a 5 minute baseline period) and by measuring the subsequent outward shift in $I_{holding}$ following Gabazine chase (mean $I_{holding}$ from last 2 minutes of Gabazine wash-on – mean $I_{holding}$ from last 2 minutes of THIP wash-on). We normalized changes in $I_{holding}$ to the membrane capacitance (Cm = Tm/Rm) of each cell. We measured Tm from a double-exponential fit to the decay phase (peak + 15 ms) of membrane capacitive transients evoked by -5 mV steps in the holding potential. We used the formula Tm = (A1/(A1+A2))*T1) + ((A2/(A1+A2))*T2), where A refers to the amplitude and T refers to the decay time constant of the two exponentials.

Behavioral Seizures

Flurothyl-induced seizures. We performed flurothyl (bis(2,2,2-trifluoroethyl) ether) seizure experiments in a ventilated chemical hood, testing mice individually within an air-tight glass chamber (~ 2 L in volume). We allowed mice to habituate to the chamber for 1 minute prior to the administration of 10% flurothyl in 95% ethanol, which we infused through a 5 ml syringe onto a gauze

pad suspended at the top of the chamber at a rate of 200 μl/min. We recorded resultant seizure behaviors using a video camera and scored the following events blind to genotype: 1) latency to the first myoclonic jerk (i.e., brief, but severe, contractions of the neck and body musculature occurring while the mouse maintains postural control); 2) latency to the first generalized seizure (i.e., convulsions resulting in a loss of postural control). Upon observation of a generalized seizure, we immediately removed the lid of the chamber, exposing the mouse to fresh air, thereby facilitating cessation of the seizure. We cleaned the chamber with 70% ethanol and replaced the gauze pad between trials.

Audiogenic Seizures. We modeled our audiogenic seizure experiments after those described in a previous study (Michalon et al., 2012). We tested P70-P100 mice that were backcrossed 6-7 generations onto the 129S2/SvPasCrl background to enhance the penetrance of audiogenic seizure phenotypes. Following 1 minute of habituation to the behavioral chamber, we exposed mice to 30 seconds of loud sound (~125 dB) emitted by two simultaneously triggered personal alarm sirens (49-1010, RadioShack, Fort Worth, TX). We video-recorded each session and scored seizure severity blind to genotype.

qRT-PCR

For quantitative reverse transcriptase polymerase chain reaction (qRT–PCR) analysis, we extracted total RNA from the neocortices of ~P60 mice using Invitrogen TRIzol reagent (Life Technologies, Grand Island, NY). We then performed first strand cDNA synthesis on 500 ng–2 μg total RNA per sample using Invitrogen Superscript III reverse transcriptase (Life Technologies) primed with random hexamers. We used Invitrogen SYBR green (Life Technologies) for all qPCR reactions, which were run on a Rotorgene 3000 (Corbett Research, Sydney, Australia). We generated standard curves and C_t values using Rotorgene analysis software version 6.0, and we determined expression of *Ube3a* after normalization of each complementary DNA sample to expression levels of the

housekeeping gene *Rpl22*. Primers were as follows: *Ube3a* F (5′-CAAAAGGTGCATCTAACAACTCA-3′), *Ube3a* R (5′-GGGGAATAATCCTCACTCTCTC-3′), *Rpl22* F (5′- AAGAAGCAGGTTTTGAAG-3′), and *Rpl22* R (5′-TGAAGTGACAGTGATCTTG-3′).

Western Blotting

We anesthetized mice with sodium pentobarbital (40 mg/kg i.p.) prior to decapitation and brain removal. We then rapidly dissected the neocortical hemispheres in ice-cold PBS, snap-froze them with liquid nitrogen, and stored them at -80°C. Using a glass tissue homogenizer (Wheaton, Millville, NJ), we homogenized frozen tissue samples with ice-cold RIPA buffer (50 mM Tris pH 8.0, 150 mM NaCl, 1% triton x-100, 0.1% SDS, 0.5% Na Deoxycholate) supplemented with 2 mM EDTA and a protease inhibitor cocktail (Sigma, Saint Louis, MO). We cleared homogenates via 16,000 x g centrifugation for 20 minutes at 4°C and we determined protein concentrations of the supernatants using the BCA assay (Thermo Scientific, Waltham, MA). Next, we resolved protein samples (30 µg per lane) by SDS-PAGE and transferred them to nitrocellulose membranes. We blocked membranes for 1 hour at room temperature in Odyssey blocking buffer (Li-COR, Lincoln, NE) prior to incubation overnight at 4°C with primary antibodies diluted in a 1:1 solution of blocking buffer and Tris-buffered saline containing 0.1% Tween-20 (TBST). We used the following primary antibodies: 1:1,000 mouse anti-UBE3A (Sigma-Aldrich Cat# E8655, RRID:AB_261956) and 1:5,000 mouse anti-GAPDH (Millipore Cat# MAB374, RRID:AB_2107445). We subsequently washed membranes with TBST prior to incubation for 1 hour at room temperature with donkey anti-mouse 800CW (LI-COR Biosciences Cat# 926-32212, RRID:AB_621847) diluted 1:10,000 in the same diluent as the primary antibodies. Finally, we repeatedly washed blots in TBST followed by TBS alone prior to imaging with the Odyssey imaging system (LI-COR).

Immunohistochemistry

For Light Microscopy. We anesthetized mice with sodium pentobarbital (40 mg/kg) prior to transcardial perfusion with phosphate-buffered saline (PBS), immediately followed by phosphate-buffered 4% paraformaldehyde (pH 7.3). We removed perfused brains from their skulls and postfixed them overnight at 4°C prior to sequential 12-hour incubations in 10%, 20%, and 30% sucrose in PBS (pH 7.5) for cryoprotection. We then froze cryoprotected brains on dry ice and cut them into 40 µm-thick sections with a sliding microtome (Thermo Scientific). We stored sections at -20°C in a cryopreservative solution (by volume: 45% PBS, 30% ethylene glycol, 25% glycerol) until free-floating immunohistochemical processing.

For immunofluorescent staining, we rinsed sections several times in PBS before blocking in PBS plus 5% normal goat serum and 0.2% Triton-X-100 (NGST) for 1 hour at room temperature. We subsequently incubated blocked tissue sections in primary antibodies diluted in NGST for 48 hours at 4°C. We then rinsed them several times in PBS containing 0.2% Triton-X-100 (PBST) before incubation in secondary antibodies (also diluted in NGST) for 1 hour at room temperature. Primary antibodies used: 1:1,000 mouse anti-UBE3A (Sigma-Aldrich Cat# SAB1404508, RRID:AB_10740376), 1:500 mouse anti-NeuN (Millipore Cat# MAB377, RRID:AB_10048713), 1:2,000 mouse anti-parvalbumin (235, Swant, Marly, Switzerland), 1:500 rabbit anti-parvalbumin (PV-25, Swant), 1:1,000 rabbit anti-calretinin (7699/4, Swant), 1:500 rat anti-somatostatin (Millipore Cat# MAB354, RRID:AB_2255365), 1:1,000 rabbit anti-somatostatin (Bachem Cat# T-4103.0050, RRID:AB_518614), and 1:500 rabbit anti-Cux1 (Santa Cruz Biotechnology Cat# sc-13024, RRID:AB_2261231). We used secondary antibodies (Thermo Fisher Scientific) at a 1:500 dilution, including Alexa-488 goat anti-mouse IgG_{2a} (Cat# A21131, RRID:AB_10562578), Alexa-647 goat anti-mouse IgG_1 (Cat# A21240, RRID:AB_10565021), Alexa-568 goat anti-mouse IgG_1 (Cat# A21124, RRID:AB_10562737), Alexa-633 goat anti-mouse IgG (Cat# A21052, RRID:AB_10584496), Alexa-488 goat anti-rabbit IgG (Cat# A11008, RRID:AB_10563748), Alexa-568 goat anti-rabbit IgG (Cat#

A11011, RRID:AB_10584650), Alexa-633 goat anti-rabbit IgG (Cat# A21070, RRID:AB_10562894), and Alexa-568 goat anti-rat IgG (Cat# A11077, RRID:AB_10562719). We stained all brain sections compared within figures in the same experiment, under identical conditions.

For Electron Microscopy. We anesthetized mice with sodium pentobarbital (40 mg/kg) prior to transcardial perfusion with 0.9% saline solution for 1 min, followed by a mixture of depolymerized 2% paraformaldehyde and 2% glutaraldehyde (Electron Microscopy Science, Hatfield, PA) in 0.1 M phosphate buffer, pH 6.8. We then postfixed brains overnight in the same fixative before preparing 50 µm-thick sections on a vibratome. Next, we incubated vibratome sections in 1% osmium tetroxide in 0.1 M phosphate buffer (pH 6.8), followed by rinsing in 0.1 M maleate buffer (pH 6.0), before incubation in 1% uranyl acetate in maleate. We then dehydrated the sections in ethanol, infiltrated them with Spurr resin, and flat-embedded them between sheets of ACLAR plastic to create wafers, which we heat-polymerized. We cut chips of tissue from the wafers and glued them to plastic blocks to support the cutting of ~70 nm-thick sections, which we collected on copper mesh grids and poststained with uranyl acetate and Sato's lead.

We performed postembedding immunocytochemistry as previously described (Phend et al., 1992). Briefly, we pre-treated grids by incubating them at 60°C in 0.01M citrate buffer (pH 6.0) for 15 mins before blocking with 1% bovine serum albumin in Tris-buffered saline with 0.005% Tergitol NP-10 (TBSN, pH 7.6). We then incubated the grids overnight at 21–24 °C in rabbit anti-GABA antibody (Sigma-Aldrich Cat# A2052, RRID:AB_477652), diluted 1:100,000. Grids were rinsed, blocked in 1% normal goat serum in TBSN (pH 8.2), and incubated for 2 hours in goat anti-rabbit antibodies conjugated to 20 nm gold particles (EM.GAR20, BBI Solutions, Madison, WI). Finally, we rinsed the stained grids and then counterstained them with 1% uranyl acetate followed by Sato's lead.

Imaging and Figure Production

We acquired images of immunofluorescently stained brain sections with a Zeiss LSM 710 confocal microscope equipped with ZEN imaging Software (Zeiss, Jena, Germany, RRID:SCR_013672). We collected images compared within figures during the same imaging session using identical acquisition parameters. We collected all electron micrographs with a Tecnai electron microscope (Phillips, Andover, MA) at 80 KV. Occasionally, images were linearly adjusted for brightness and contrast using Image J software (RRID:SCR_003070) (Schneider et al., 2012). All images to be quantitatively compared underwent identical manipulations. We prepared all figures using Adobe Illustrator software (Adobe Systems Inc., San Jose, CA, RRID:SCR_010279).

Quantification of Neuron Density and Cre Recombination Efficiency

We acquired all images to be analyzed for interneuron density or Cre recombination efficiency using thin (1.4 μm-thick) optical sectioning. We quantified PV^+, CRT^+, and SOM^+ interneuron density from 5 strips (500 μm-wide) of primary visual cortex per mouse imaged at ~P80. We determined the efficiency of AAV-Cre-mediated deletion of maternal *Ube3a* by analyzing UBE3A colocalization in $tdTomato^+$ cells from 800 μm-wide strips of primary visual cortex imaged from P12 mice. We analyzed a total of 246 tdTomato+ cells from *Ube3a*$^{m+/p+}$ mice (5 images) and 337 $tdTomato^+$ cells from *Ube3a*$^{FLOX/p+}$ mice (10 images).

Statistical Analyses

Composition of experimental "Control" groups:

Figures S3, S4, and S7: *Ube3a*$^{m+/p+}$ and *Ube3a*$^{m+/p+}$*::Nestin-Cre*.

Figures 1, 4D, 5C, 5D, 6B, 7A, S2, and S8A-C: *Ube3a*$^{m+/p+}$, *Ube3a*$^{FLOX/p+}$, and *Ube3a*$^{m+/p+}$*::Gad2-Cre*.

Figures 3E-G, and 4C: *Ube3a*$^{m+/p+}$, *Ube3a*$^{FLOX/p+}$, and *Ube3a*$^{m+/p+}$*::NEX-Cre*.

Figures 2, 5B, 6C, 7B, S5, and S8D-F: *Ube3a*$^{m+/p+}$ and *Ube3a*$^{m+/p+}$*::Gad2-Cre*.

Figure 3C: *Ube3a*$^{m+/p+}$ and *Ube3a*$^{m+/p+}$*::NEX-Cre*.

Statistical analyses by experiment:

Interneuron density: 2-way ANOVA with Sidak's *(*Figure S2A) or Tukey's (Figure S4A) post-hoc test.

AAV-Cre-mediated recombination efficiency: Unpaired, 2-tailed student's t-test (Figure S6A$_4$).

mIPSCs and mEPSCs: 1-way ANOVA with Tukey's post-hoc test *(*Figures S4B, S4C, and S5A-C) and unpaired, 2-tailed student's t-test (Figures 1C, 3F, and S2B).

Paired-pulse: Kruskal-Wallis test (Figure S4E), 1-way ANOVA with Tukey's post-hoc test (Figure S5D) and unpaired, 2-tailed student's t-test (Figure S2C).

Input-output: 2-way repeated measures ANOVA with either Tukey's (Figures 2C, 3C, S4D and S6B) or Sidak's (Figures 1D and 3E) post-hoc test.

Recovery from high-frequency synaptic depletion: 1-way ANOVA with Tukey's post-hoc test (Figures 2D, S4F, and S5E) or unpaired, 2-tailed student's t-test (Figure 1E), each comparing the last 108 seconds of the recovery phase.

Flurothyl-induced seizures: Unpaired, 2-tailed student's t-test (Figure 4C and 4D$_1$-D$_2$).

Flurothyl survival: Log-rank (Mantel-Cox) test (Figure 4D$_3$).

Post-weaning lethality: Chi-square test (Figure 5D).

Audiogenic seizures: Chi-square test (Figure 5B and 5C).

LFP spectral power: Unpaired, 2-tailed student's t-test (Figure 6B$_3$) or 1-way ANOVA with Tukey's post-hoc test (Figure 6C$_3$) of delta power band.

Ultrastructural analyses of presynaptic terminals: Unpaired, 2-tailed student's t-test (Figures 7A$_3$-A$_5$ and S8A-C) or 1-way ANOVA with Tukey's post-hoc test (Figures 7B$_4$-B$_6$, S7B-D, and S8D-F).

SUPPLEMENTAL REFERENCES

Berrios, J., Stamatakis, A.M., Kantak, P.A., McElligott, Z.A., Judson, M.C., Aita, M., Rougie, M., Stuber, G.D., and Philpot, B.D. (2016). Loss of UBE3A from TH-expressing neurons suppresses GABA co-release and enhances VTA-NAc optical self-stimulation. Nat Commun *7*, 10702.

Goebbels, S., Bormuth, I., Bode, U., Hermanson, O., Schwab, M.H., and Nave, K.A. (2006). Genetic targeting of principal neurons in neocortex and hippocampus of NEX-Cre mice. Genesis *44*, 611-621.

Gray, S.J., Foti, S.B., Schwartz, J.W., Bachaboina, L., Taylor-Blake, B., Coleman, J., Ehlers, M.D., Zylka, M.J., McCown, T.J., and Samulski, R.J. (2011). Optimizing promoters for recombinant adeno-associated virus-mediated gene expression in the peripheral and central nervous system using self-complementary vectors. Hum Gene Ther *22*, 1143-1153.

Jiang, Y.H., Armstrong, D., Albrecht, U., Atkins, C.M., Noebels, J.L., Eichele, G., Sweatt, J.D., and Beaudet, A.L. (1998). Mutation of the Angelman ubiquitin ligase in mice causes increased cytoplasmic p53 and deficits of contextual learning and long-term potentiation. Neuron *21*, 799-811.

Madisen, L., Zwingman, T.A., Sunkin, S.M., Oh, S.W., Zariwala, H.A., Gu, H., Ng, L.L., Palmiter, R.D., Hawrylycz, M.J., Jones, A.R.*, et al.* (2010). A robust and high-throughput Cre reporting and characterization system for the whole mouse brain. Nat Neurosci *13*, 133-140.

Michalon, A., Sidorov, M., Ballard, T.M., Ozmen, L., Spooren, W., Wettstein, J.G., Jaeschke, G., Bear, M.F., and Lindemann, L. (2012). Chronic pharmacological mGlu5 inhibition corrects fragile X in adult mice. Neuron *74*, 49-56.

Phend, K.D., Weinberg, R.J., and Rustioni, A. (1992). Techniques to optimize post-embedding single and double staining for amino acid neurotransmitters. J Histochem Cytochem *40*, 1011-1020.

Philpot, B.D., Espinosa, J.S., and Bear, M.F. (2003). Evidence for altered NMDA receptor function as a basis for metaplasticity in visual cortex. J Neurosci *23*, 5583-5588.

Schneider, C.A., Rasband, W.S., and Eliceiri, K.W. (2012). NIH Image to ImageJ: 25 years of image analysis. Nat Methods *9*, 671-675.

Silva-Santos, S., van Woerden, G.M., Bruinsma, C.F., Mientjes, E., Jolfaei, M.A., Distel, B., Kushner, S.A., and Elgersma, Y. (2015). Ube3a reinstatement identifies distinct developmental windows in a murine Angelman syndrome model. J Clin Invest *125*, 2069-2076.

Taniguchi, H., He, M., Wu, P., Kim, S., Paik, R., Sugino, K., Kvitsiani, D., Fu, Y., Lu, J., Lin, Y.*, et al.* (2011). A resource of Cre driver lines for genetic targeting of GABAergic neurons in cerebral cortex. Neuron *71*, 995-1013.

Tronche, F., Kellendonk, C., Kretz, O., Gass, P., Anlag, K., Orban, P.C., Bock, R., Klein, R., and Schutz, G. (1999). Disruption of the glucocorticoid receptor gene in the nervous system results in reduced anxiety. Nat Genet *23*, 99-103.